

Rijksuniversiteit Groningen

Faculteit der Wiskunde en Natuurwetenschappen

Lifetime of Paraexcitons in Cuprous Oxide



RUG

**Zernike Institute
for Advanced Materials**

MASTER THESIS BY: Marian Otter

Research Group: Optical Condensed Matter Physics

Supervisor: D.A. Fishman, Prof. dr. ir. P.H.M. van Loosdrecht

Referent: Dr. B. de Boer

Period: September 2006 – Augustus 2007

Abstract

We studied lifetime, luminescence, vacancies and differential transmission of ortho and paraexcitons in different samples of Cu_2O . The radiative decay of orthoexcitons to the ground state is phonon-assisted. Paraexcitons decay by thermal upconversion to orthoexcitons. In our luminescence experiment the temperature of the exciton gas is 80-85 K for most samples for a lattice temperature of 77 K. A reason for differences in exciton lifetime for different samples is the difference in the amount of copper vacancies. We found no correlation between oxygen vacancy concentration and exciton lifetime. Measurements show that the vacancy concentration severely influences the lifetime of the excitons, because of the high diffusion constant (about $1000 \text{ cm}^2/\text{s}$ at 1.2 K) of excitons in Cu_2O . We measured lifetimes ranging from ns to μs . In our experiments, the highest exciton density created is about 10^{17} cm^{-3} . For this density we need a temperature of about 2 K to reach Bose-Einstein condensation.

Contents

1	Introduction	5
2	Theory	11
2.1	Exciton model	11
2.2	Exciton creation and recombination	13
2.3	Selection rules	16
2.4	Vacancy concentration	19
2.5	Diffusion	22
2.6	Luminescence - temperature dependence	23
2.6.1	Energy shift of bandgap	23
2.6.2	Energy shift of 1s-2p transition	24
2.6.3	Linewidth of the emission spectrum	25
2.7	Induced absorption	29
2.8	Exciton density	31
3	Experimental setup	33
3.1	Visible pump - infrared probe measurements	33
3.2	Time-resolved luminescence	35
3.3	CW spectroscopy	38
3.3.1	Description of the setup	38

3.3.2	Probe and pump pulse modulation	41
4	Results and discussion	45
4.1	Lifetime	45
4.2	Luminescence	49
4.3	Differential transmission	51
4.4	Vacancy measurements	58
4.5	Exciton density	64
5	Conclusion	67
6	Acknowledgements	71
	Bibliography	75
A	Luminescence	79
B	Vacancies	83
C	Differential transmission	87

Chapter 1

Introduction

Cuprous oxide is a direct bandgap semiconductor that has been studied experimentally and theoretically for many years now [1]. It was the first material in which an exciton gas was observed [2]. It has been studied for decades due to its promise as a host for a Bose-Einstein condensate of excitons ([3],[4],[5]). For this two main conditions should be fulfilled: a high density of excitons and a low excitonic temperature. That is why yellow paraexcitons, the lowest energy excitonic state in Cu_2O , are very interesting; the transition from the paraexciton level to the ground state is forbidden to all orders, so they are expected to have a very long lifetime. Lifetimes in the order of ns, μs and ms have been measured ([6],[1], [7]).

A lot of work has been done to explore the properties of excitons. Also different ways of creating excitons have been discovered. An exciton is an electron-hole pair kept together by the Coulomb energy. In cuprous oxide the exciton has a Bohr radius of 7 Å and an unusually high binding energy of 150 meV [8]. This is the binding energy of the 1s exciton, which is exceptional; starting at the 2p level, a Rydberg series of hydrogenlike states of the electron and hole can be observed. All energy levels, except for the 1s exciton level, can be calculated with the formula

$E_n = E_g - \Delta E/n^2$ where $E_g = 2.17$ eV is the bandgap energy and $\Delta E = 98.5$ meV is the excitonic Rydberg energy [9].

The exciton states are split by spin-orbit coupling. The 1s state is split into a singlet state, the paraexciton, and a triplet state, the orthoexciton. The orthoexciton lifetime is limited by conversion to the paraexciton state, which happens in about 3 ns in a crystal at 2 K [10]. Also orthoexciton decay to the groundstate is quadrupole allowed. The timescale for this transition is at least 25 μ s [11]. Another path for orthoexcitons to decay is via impurities and defects. The importance of Auger recombination, the collision of two excitons in which the nonradiative recombination of one electron-hole pair transfers kinetic energy to the remaining electron and hole, is still under debate [7]. The lifetime of the paraexciton is mainly limited by nonradiative recombination at impurities and defects.

Since excitons are a bound state of two fermions, they are expected to obey Bose statistics. In thermal equilibrium, we expect the occupation number of the exciton kinetic energy eigenstate with energy ϵ to be given by the Bose-Einstein distribution, $f(\epsilon) = 1/[\exp[(\epsilon - \mu)/k_B T] - 1]$, where μ is the chemical potential and T is the temperature of the exciton gas. The Bose statistics of excitons should become noticeable in their equilibrium distribution when the exciton density is sufficiently large, because then the low- ϵ occupation numbers become large ($V/n\lambda_B^3 \leq 1$, where V is the volume, n is the number of particles and λ_B is the de Broglie wavelength). Theory predicts that Bose-Einstein condensation can occur at any temperature, as long as the density is high enough. The critical density for BEC of noninteracting bosons is given by the equation [12]:

$$n_c = 2.612g \left(\frac{mk_b T}{2\pi\hbar^2} \right)^{3/2} \quad (1.1)$$

where g is the degeneracy of the level, and m is the exciton mass, which for the 1s state is $2.7 m_0$, where m_0 is the electron rest mass. Taking into account reasonable

pump intensities and purity of the samples the possible densities are in the order of 10^{18} to 10^{19} cm^{-3} . Based on equation 1.1 the required density is about 10^{17} cm^{-3} at a gas temperature of 2 K. This can be seen in figure 1.1. Because the energy of the photons absorbed is higher than the energy needed to create an exciton, hot excitons are created. The long lifetime of the paraexciton state allows cooling of the exciton gas towards the lattice temperature, and helps to reach a sufficiently high density for Bose-Einstein condensate formation. For orthoexcitons the particle loss is faster than the cooling rate [8], which prevents the forming of a BEC.

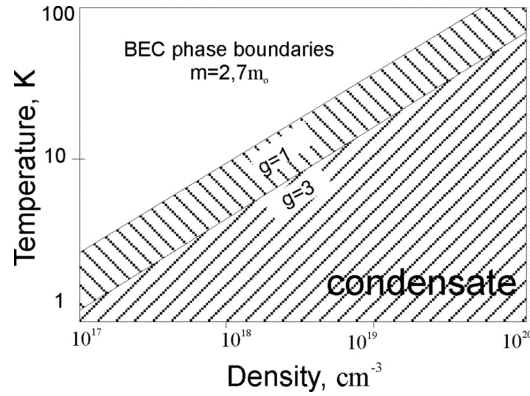


Figure 1.1: Phase diagram for ortho ($q=1$) and para ($q=3$) excitons in Cu_2O . The transition temperature to a condensate is shown as a function of density. For the calculation exciton - exciton interactions are not taken into account. For paraexcitons (spins parallel, nondegenerate) the density needed for $T = 2$ K is about 10^{17} cm^{-3} .

The paraexciton, with its long lifetime, cannot be probed by measuring direct luminescence. As was reported in other works ([14],[15],[16]), it is possible to probe the population of the 1s paraexcitons via laser induced changes in the absorption in the infrared region caused by the presence of excitons. First excitons are created by a one or two-photon excitation process through excitation of an electron from the

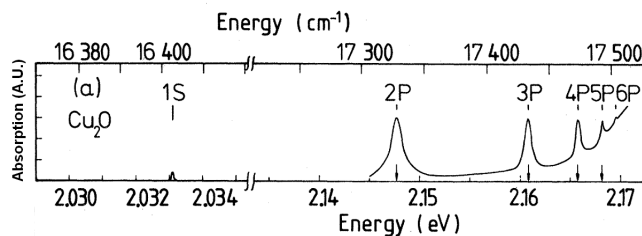


Figure 1.2: Position of different exciton energy levels for the yellow exciton in Cu_2O . For p-states the splitting of the para and ortho exciton state is small and not visible in the figure. Figure taken from [13].

valence to the conduction band, ending up in the 1s state. These excitons can make transitions to different higher energy levels, comparable to the hydrogen atom. The energies of different energy levels are indicated in figure 1.2.

In order to determine the exciton density, one can measure the absorption strength of one of the transitions. The more infrared light is absorbed, the higher the exciton density. In our project the infrared pulse used to make such a transition has an energy with the peak position around 129 meV. With this pulse, excitons can be excited from the 1s-para level to the 2p-para level. The energy of the 1s-ortho to 3p-ortho transition lies close to the 1s-para to 2p-para transition. These two transitions appear in the spectrum as one broad peak. By changing the probe wavelength, other transitions can be measured as well.

When temperature-induced spin-flip occurs, paraexcitons are upconverted to orthoexcitons and can radiatively decay to the groundstate. This allows to measure the lifetime of paraexcitons at 77 K by recording the decay of the orthoexciton luminescence signal in time. The decay is phonon-assisted with a phonon energy of 13.6 meV. Also we measured the vacancy concentration of few samples by looking at the luminescence, caused by excitons trapped by oxygen and copper vacancies. We compared the luminescence, vacancy concentration and differential transmission

spectra for samples with a long exciton lifetime (in the order of μs) and samples with a short exciton lifetime (in the order of 10 ns). We show that the copper vacancy concentration is much higher for short lifetime samples. These experiments were done in collaboration with the Gonokami group at the University of Tokyo. For reaching BEC, the main goal of this field, we show that copper vacancies should be avoided when growing Cu_2O samples, because they decrease the exciton lifetime. Finally, we show that we can create a density of excitons which theoretically should be high enough to reach BEC at 2 K.

Chapter 2

Theory

2.1 Exciton model

An exciton is a bound electron-hole pair. It is bound by the Coulomb interaction. This system can be modelled as a hydrogen-like atom. The size of the exciton is described by the Bohr radius:

$$\alpha = \frac{\hbar^2}{\mu(e^2/\epsilon)} \quad (2.1)$$

In this equation e is the elementary electronic charge, ϵ is the dielectric constant and μ is the reduced mass. The radius for energy levels, except for the lowest one, is proportional to the square of the principal quantum number n , $r = n^2\alpha$. Confusedly, some authors also refer to r as the Bohr radius. In Cu_2O the Bohr radius is about 5.3 \AA for the lowest energy excitonic level, while r is 7 \AA . This is the only energy level for which the proportionality of the radius to n^2 does not hold. For other excitonic levels the Bohr radius is about 1.1 nm .

Two types of excitons exist. Frenkel excitons have a Bohr radius in the order of the lattice constant or smaller. Such an exciton is strongly bound and is usually localized on one site. The electron and hole do not move independently. A Wannier

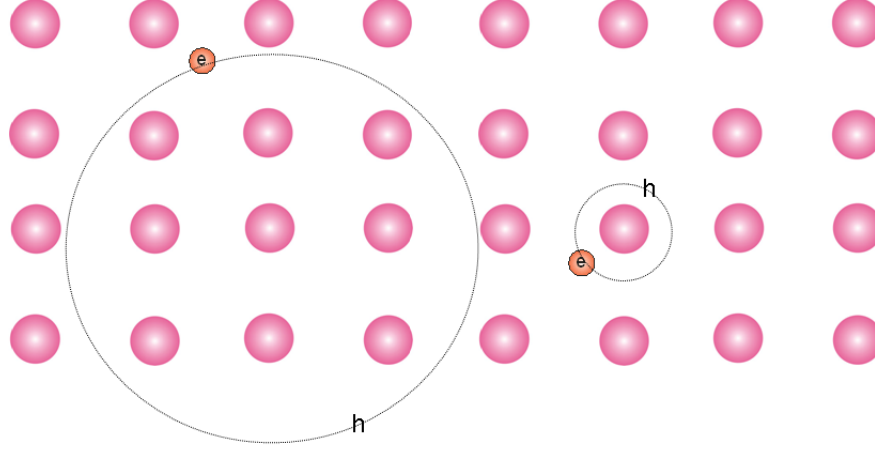


Figure 2.1: Schematic illustration of exciton types. Left: Wannier exciton. The Bohr radius is larger than the lattice constant, which means that there are atoms inside the excitonic radius. Right: Frenkel exciton. The size of the Bohr radius is smaller than the lattice constant.

exciton is weakly bound and delocalized over a number of sites, ie the Bohr radius is larger than the lattice constant. Both electron and hole are mobile. For this type of exciton there are atoms inside the exciton orbit which causes screening of the Coulomb interaction: $-e^2/r^2 \rightarrow -e^2/\epsilon r^2$, leading for instance equation 2.1. The Frenkel and Wannier exciton are depicted in figure 2.1.

In Cu_2O the lattice constant is 4.3 \AA , which is in the order of the Bohr radius of the 1s state, so we have Frenkel-like excitons for the lowest energy level. Excitons with higher energy become more Wannier-like. For example, the p-states have a bohr radius of about 1.1 nm [16]. We can use a simple two-particle model to describe the binding energy of this Wannier exciton. The electron is excited from the valence band to the conduction band leaving a hole in the valence band. The electron and hole can be treated as two weakly interacting particles with mass m_e^* and m_h^* ,

respectively. The Hamiltonian can be written as [17]:

$$H = -\frac{\hbar^2 \nabla_e^2}{2m_e^*} - \frac{\hbar^2 \nabla_h^2}{2m_h^*} - \frac{e^2}{\epsilon |r_e - r_h|} + \frac{\hbar^2 l(l+1)}{2\mu r^2} \quad (2.2)$$

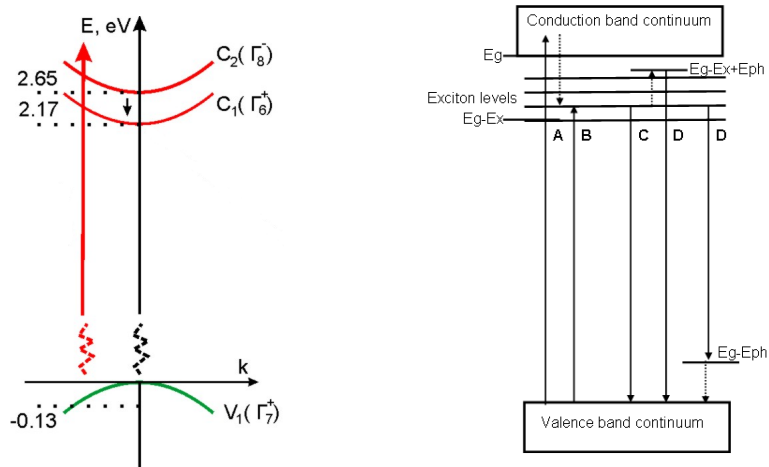
The positions of electron and hole are given by r_e and r_h , respectively. The corresponding eigenvalues for equation 2.2 form a series of exciton energies given by:

$$\begin{aligned} E_n &= E_G - \frac{\mu(e^2/\epsilon)^2}{2\hbar^2 n^2} + \frac{\hbar^2 k^2}{2M} + \frac{\hbar^2 l(l+1)}{2\mu r^2} \\ \frac{1}{\mu} &= \frac{1}{m_e^*} + \frac{1}{m_h^*} \\ M &= m_e^* + m_h^*. \end{aligned} \quad (2.3)$$

Here E_G is the band gap energy, n is the principal quantum number and l is the angular momentum quantum number. The top of the valence band is defined as the zero level. The second term is the exciton binding energy which is 150 meV for the lowest exciton energy level in Cu_2O , the third term is the exciton kinetic energy, and the fourth term is the splitting of the levels into states with different angular momentum l . From this formula we see that a series of sharp peaks can be expected in the exciton emission and absorption spectra. In analogy with the hydrogen atom, the levels are labelled nl , so the ground level is 1s, the first excited level 2p, and so on. This can be seen in figure 1.2.

2.2 Exciton creation and recombination

In figure 2.2 the band structure of Cu_2O near the Γ -point (the center of the Brillouin zone) is shown. An electron from the valence band can be excited directly into an excitonic state (process B) or to a conduction band (process A). In the latter case an electron-hole pair is created. If this pair dissipates the extra energy radiatively or non-radiatively, a bound exciton state is formed. Excitation can be done by absorption of one or more photons. Different decay processes can occur. Direct radiative



(a) Bandstructure of Cu_2O . The exciton 1s level lies 150 meV below the first conduction band.

(b) Different ways of exciton creation are possible: process A, an electron is excited from the valence band to a conduction band. It may decay either radiatively or non-radiatively to an excitonic state. Process B, direct exciton creation. Process C, direct exciton recombination. Process D, phonon-assisted recombination.

Figure 2.2: Bandstructure and exciton creation in Cu_2O .

decay occurs when the exciton recombines by emitting a photon (process C). The energy of the emitted photon is then equal to the exciton energy. The emission may also occur together with the emission or absorption of a phonon (process D). Also, the exciton may decay non-radiatively (for instance Auger decay). For orthoexcitons the main decay process is conversion to paraexcitons. For paraexcitons the main decay process is trapping at impurities. Another way to lose paraexcitons is by thermal upconversion to orthoexcitons.

The energy of the photon when direct recombination occurs can be written as:

$$h\nu = E_G - E_x + E_k \quad (2.4)$$

where E_x is the exciton binding energy and E_k is the exciton kinetic energy. Similarly, the photon energy when phonon-assisted recombination occurs can be written as:

$$h\nu = E_G - E_x + E_k \pm E_p \quad (2.5)$$

where E_p is the phonon energy. The '+' corresponds to the creation of a phonon and the '-' to annihilation. Momentum conservation requires that only two types of processes are possible: $k = k_{\text{photon}}$ for direct transitions and $k = k_{\text{photon}} + k_{\text{phonon}}$ for phonon-assisted transitions.

When electron-hole pairs are formed, they are in a non-equilibrium situation. In about 200 fs they reach an equilibrium electronic temperature via optical phonon emission [8]. This temperature is higher than the lattice temperature. Cooling towards the lattice temperature is achieved by emission of acoustical phonons. The lattice temperature can only be reached if the thermalization time is at least a few times shorter than the lifetime of the excitons.

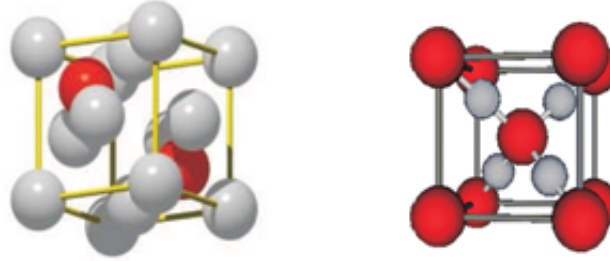


Figure 2.3: Left: the FCC sublattice of copper. Right: the BCC sublattice of oxygen. A red ball represents oxygen and a grey one copper.

2.3 Selection rules

Cuprous oxide is a direct gap semiconductor with a cubic structure. It consists of two sublattices: a copper sublattice of FCC type and an oxygen sublattice of BCC type. This is shown in figure 2.3.

Cuprous oxide has several excitonic series in the energy range of the visible light. These are shown in figure 2.4. The yellow series are derived from the highest valence band and the lowest conduction band ($V_1 - C_1$). The green series is related to the gap $V_2 - C_1$, the blue series to $V_1 - C_2$ and the indigo series to the gap $V_2 - C_2$. Some parameters of Cu_2O are indicated in the table below.

lattice constant	4.26 Å
smallest direct optically forbidden gap	2.17 eV
exciton binding energy (1s yellow state)	150 meV
ground state Bohr radius	7 Å
exciton mass	$2.7 m_e$
ortho-para level splitting energy	12 meV

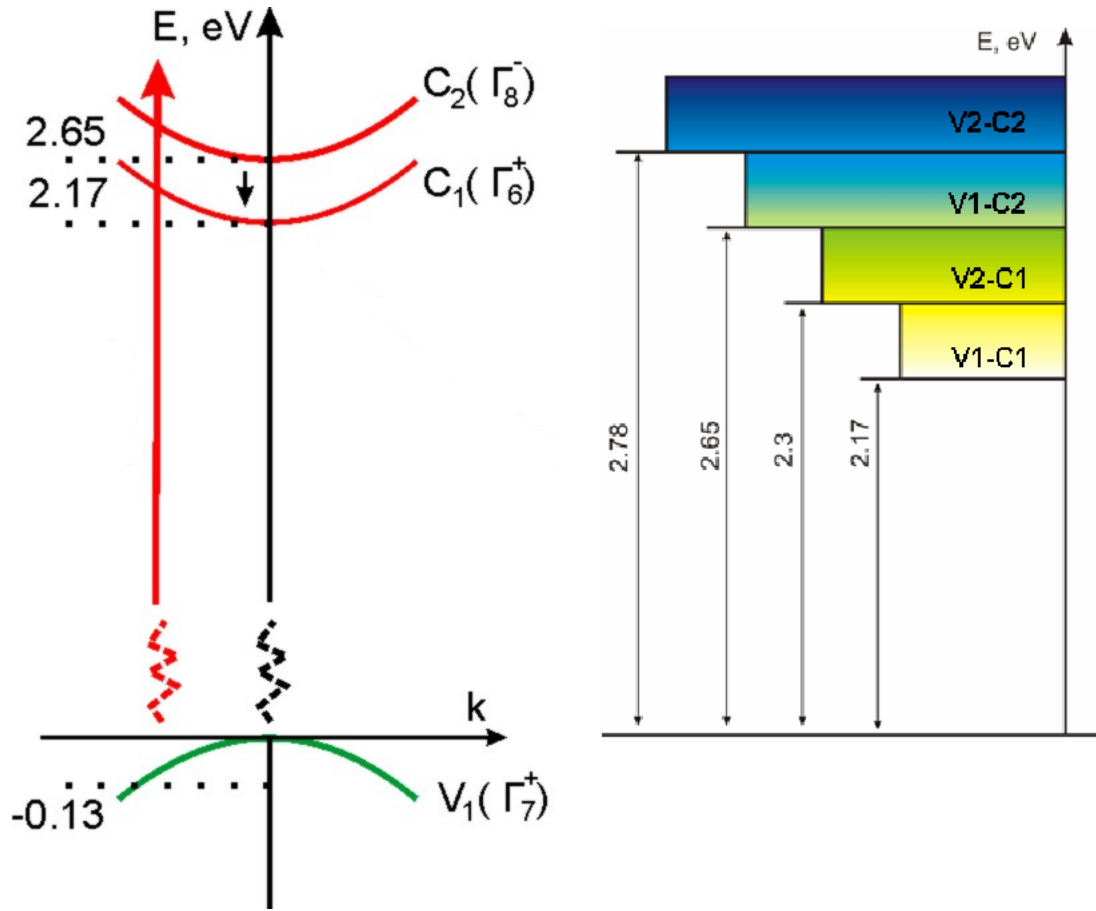


Figure 2.4: The energies of the different possible optical transitions between conduction bands C_1 and C_2 and valence bands V_1 and V_2 .

For the yellow series the energy gap is direct, but dipole forbidden. To see if a transition can be made we should calculate the absorption coefficient, which is proportional to $\sum_i \langle \Gamma_f^\pi | D_i | \Gamma_i^\pi \rangle$, where $\Gamma_{f(i)}^\pi$ is the final (initial) state with parity π and $D_i \propto p_i$ for the dipole operator and $D_i \propto p_i^2$ for the quadrupole operator [18]. Here p_i are operators \hat{x}, \hat{y} and \hat{z} in three dimensions. We assume a direct transition. For Cu_2O the lowest conduction band and highest valence band have the same, positive, parity. The dipole operator has a negative parity. When we integrate over space, the absorption coefficient will always be zero. The quadrupole operator has a positive parity. This means that the matrix element can be non-zero, which is the case for the $V_1 - C_1$ transition.

For excitonic levels the total parity is determined by the product of the parities of the valence band, conduction band and exciton level. Since both valence band and conduction band have a positive parity, this means that the total parity is determined by the parity of the exciton level. For a s-level, the parity is positive, and transitions to the ground state are dipole forbidden but quadrupole allowed. For a p-level, the parity is negative, and transitions to the ground state are dipole allowed. Due to spin-orbit coupling, every excitonic level is split into an ortho level with symmetric wavefunction ($J=1$) and a para level with anti-symmetric wavefunction ($J=0$). For the 1s level the difference in energy is 12 meV. Because only transitions between levels can be made when $\Delta L = \pm 1$, decay from any para level to the ground state is forbidden. This means that paraexcitons can theoretically live very long. Practically, the lifetime is limited by defects and impurities. They trap the exciton in a somewhat lower energy state. The exact mechanism of trapping is still unknown. Trapped excitons can be seen in the luminescence spectrum at a somewhat lower energy. The longest paraexciton lifetimes measured are in the order of ms for a good quality sample [15]. For orthoexcitons decay to the ground state is allowed. Whether it is dipole or quadrupole allowed depends on the angular momentum of

the excitonic state. The lifetime of 1s orthoexcitons is around 1.5 ns, which is the lifetime of the transition to the lower lying paraexciton level. This transition is generally faster than the radiative transition to the ground state.

Because of the condition $\Delta L = \pm 1$, only intraexcitonic transitions of the type 1s ortho \rightarrow np ortho and 1s para \rightarrow np para can be made. The energies of these transitions lie in the infrared. The direct luminescence we measure in experiments comes from the quadrupole allowed decay of 1s-orthoexcitons to the ground state. As an example, in the table below the energies of some transitions from the 1s level to higher levels are indicated for the yellow series.

transition	exciton type	energy (meV)
1s - 2p	ortho	115.5
1s - 2p	para	127.6
1s - 3p	ortho	129.8
1s - 3p	para	140.5

2.4 Vacancy concentration

Experiments using different ways of Cu_2O crystal growth have shown that the amount of impurities in Cu_2O , for example metal particles, does not influence the lifetime and luminescence of the sample at low temperatures [19]. The reason for this can be that the capture of electrons or holes into impurity levels becomes inefficient at low temperatures. Vacancies on the other hand do have a pronounced influence on the lifetime and luminescence. Two types of vacancies occur: copper and oxygen vacancies. When an electron or hole meets a vacancy it may be trapped in the lower energy level and decay from this level to the ground state. Because of the large diffusion constant of Cu_2O , about $1000 \text{ cm}^2/\text{s}$ at 1.2 K [20], the chance of an exciton being trapped by a vacancy is large. At higher temperature more phonons

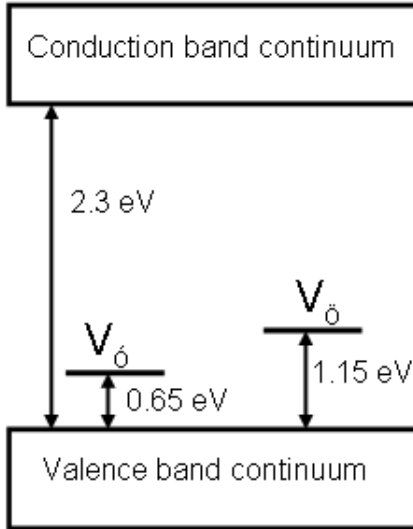


Figure 2.5: Position of the oxygen vacancy traps in Cu₂O. Energy values taken from [21].

are present leading to a slow down of exciton diffusion. Therefore the trapping of excitons will be slower at higher temperature.

Oxygen vacancies can exist in three different states: $V_{\ddot{O}}$, an anion vacancy with a double positive charge with respect to the lattice; $V_{\dot{O}}$, a vacancy which has trapped one electron and is positively charged with respect to the lattice; and V_O , a vacancy which has trapped two electrons and is neutral with respect to the lattice. The two ground energy levels of the oxygen traps, one for the $V_{\ddot{O}}$ and one for the $V_{\dot{O}}$ state, are situated above the valence band, as is depicted in figure 2.5. These traps form a bound state with one or two electrons. From this trap decay to the ground state occurs. The mechanism for this decay is not known yet. Also the optical processes involved in the mechanism are unknown.

We can characterize the amount of vacancies by looking at the strength of the

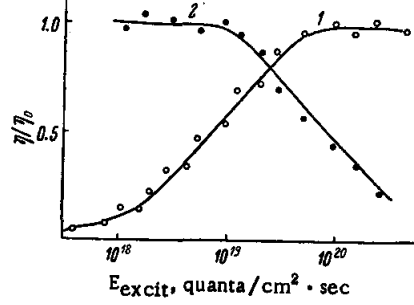


Figure 2.6: Dependence of the normalized yield of (1) λ_{720nm} and (2) λ_{820nm} luminescence on the excitation intensity. η_0 is the value of the yield corresponding to the region of linear change of intensity of the steady state luminescence with variation of E. T = 77 K. Figure taken from [22].

luminescence coming from the excitons trapped by different vacancy types. When we look at the luminescence spectra of Cu_2O [21], we see three different bands. One band is situated at 1000 nm (≈ 1.2 eV) at room temperature, shows no fine structure at 77 K and comes from copper vacancies. According to [22] the luminescence at 720 nm (≈ 1.7 eV) is emitted from the $V_{\dot{O}}^*$ state, where the asterisk denotes an excited state. This state can arise either as a result of a $V_{\dot{O}}$ center trapping an electron from the conduction band or by local excitation of a $V_{\dot{O}}$ center. The luminescence at 820 nm (≈ 1.4 eV) is emitted from a $V_{\dot{O}}^*$ state formed either as a result of trapping of an electron by a $V_{\dot{O}}$ center from the conduction band, or by local excitation of a $V_{\dot{O}}$ state. Thus a condition for the appearance of luminescence at 720 and 820 nm through local excitation is the presence of $V_{\dot{O}}$ and $V_{\dot{O}}$ centers. The condition for the appearance of this luminescence through lattice excitation is the presence of the corresponding $V_{\dot{O}}$ and $V_{\dot{O}}$ centers. Every type of center can be converted to another type by trapping of electrons or holes from the valence band.

The effect of the excitation intensity is seen in figure 2.6. It is clear that for 77 K

the yield for 720 nm, η_{720nm} increases with increasing excitation energy by at least a factor of 10, and eventually reaching a plateau. η_{820nm} is initially constant, but falls sharply with increasing excitation energy. At sufficiently high values it even completely disappears. This can be explained as follows. At 77 K there are no or very few $V_{\dot{O}}$ centers. Due to the trapping of holes, created by photoexcitation, the reaction $V_{\dot{O}} + e^+ \rightarrow V_{\dot{O}}$ occurs; also, due to thermal promotion of the electrons, the reaction $V_{\dot{O}} + e^- \rightarrow V_{\dot{O}}$ takes place. At low excitation energy the first reaction is very slow, so the number of $V_{\dot{O}}$ centers free to trap electrons according to the reaction $V_{\dot{O}} + e^- \rightarrow V_{\dot{O}}^*$ is small and η_{720nm} is small. On the other hand the presence of a large number of $V_{\dot{O}}$ centers, after electron trapping, gives rise to a large η_{820nm} according to the reaction $V_{\dot{O}} + e^- \rightarrow V_{\dot{O}}$. In addition the $V_{\dot{O}}$ centers participate in the 820 nm luminescence after trapping of a hole and subsequent trapping of an electron according to the reaction $V_{\dot{O}} + e^+ \rightarrow V_{\dot{O}} + e^- \rightarrow V_{\dot{O}}^*$.

At high excitation energies the extremely large increase in concentration of holes leads to their trapping by $V_{\dot{O}}$ and $V_{\dot{O}}$ centers predominating over the compensating trapping of thermal electrons. Almost all centers remain as $V_{\dot{O}}$ centers and consequently emit only 720 nm radiation at highest excitation energies. The region of intermediate excitation energy corresponds to a process of decrease of η_{820nm} and increase of η_{720nm} .

2.5 Diffusion

We can calculate the survival probability of an excitation diffusing with a diffusion coefficient D in a matrix of quenching sites, like vacancies or impurities. The distance between these quenching sites is approximated by a Poisson distribution with average distance L . In the limit of a high density or at long times the temporal dynamics

can be described by the equation [23]:

$$I(t) = I(0) \left(\frac{t}{\tau_{\text{diff}}} \right)^{1/2} \exp \left(-\frac{t^\beta}{\tau_{\text{diff}}^\beta} \right) \exp \left(-\frac{t}{\tau_0(t)} \right) \quad (2.6)$$

$$t \gg \frac{L^2}{\pi^2 D} \quad (2.7)$$

$$\tau_{\text{diff}} = \left[2\pi^2 \left(\frac{3^3}{2} \right) D n_{1D}^2 \right]^{-1}. \quad (2.8)$$

Here τ_{diff} is a characteristic diffusion time and $n_{1D} = (n_{3D})^{1/3}$ or $n_{1D} = 1/L$ is the one-dimensional density of quenching centers. The exponent β in the stretched exponential equals 1/3, 1/2 and 3/5 for diffusion in 1D, 2D and 3D, respectively. A time dependent exciton lifetime $\tau_0(t)$ is used to account for the multi-exponential decay of the spectral dynamics in Cu_2O . The formula consists of different parts. The last, exponential, term accounts for the decrease in intensity when no trapping occurs. The first term is related to the movement of a particle in a matrix of quenching sites as was calculated by Balagurov [24]. Finally, the middle, exponential, term accounts for the decay due to the dimensionality of the medium, which determines the exponent β .

Excitons in Cu_2O have a very high diffusion constant of about $1000 \text{ cm}^2/\text{s}$ [20]. This lead to a high dependence of the exciton lifetime on the impurity concentration. Thus it is very important to use high purity samples.

2.6 Luminescence - temperature dependence

2.6.1 Energy shift of bandgap

The excitonic emission spectrum is strongly energy dependent. The spectrum shifts due to a contraction of the bandgap when temperature increases. This can be

described by the empirical equation [25]:

$$E_G(T) = E_G(0) - \frac{\alpha T^2}{T + \beta} \quad (2.9)$$

Here α and β are constants determined by fitting and have a value of 4.8×10^{-4} eV/K and 275 K, respectively. $E_G(0)$ has a value of 2.033 eV. The equation is based on the idea that the two dominant factors contributing to the band gap temperature dependence are thermal lattice expansion and electron-phonon interactions. Both of them are a linear function of temperature at high temperature and a quadratic function of temperature at low temperature.

Another function to describe the spectrum shift which is more suitable for low temperatures is [26]:

$$E_G(T) = E_G(0) - a \left[1 + \frac{2}{e^{\theta T} - 1} \right] \quad (2.10)$$

where θ is the temperature which corresponds to the typical phonon frequency and a is the coefficient of electron-phonon coupling. In this equation it is assumed that the phonon occupation number obeys the Planck distribution. The bandgap energy change will be proportional to the phonon occupation number.

2.6.2 Energy shift of 1s-2p transition

Figure 2.7 shows the shift of the 1s-2p ortho and para transition energy as a function of energy. This shift can be explained as follows [16]: While the np ortho states shift parallel to the bandgap with increasing temperature, linear absorption and photoluminescence data reveal that the 1s-ortho exciton binding energy slightly increases by ≈ 1.5 meV from 10 to 100 K. Consequently, the nominal 1s-2p ortho transition energy shifts to the blue as well. Since the 1s ortho - 1s para splitting is expected to be temperature independent, the 1s-2p para transition shows the same blue shift.

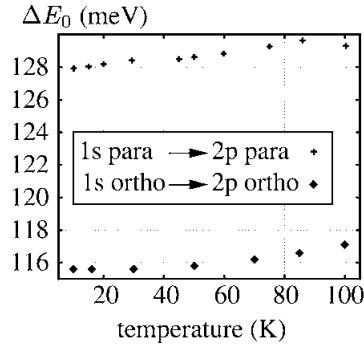


Figure 2.7: Observed 1s para - 2p para transition energy as a function of temperature compared to the nominal 1s ortho - 2p ortho transition energy extracted from linear absorption and photoluminescence. Picture taken from [16].

2.6.3 Linewidth of the emission spectrum

In Cu_2O the primary luminescence mechanism is phonon-assisted recombination of the orthoexciton involving the 13.6 meV Γ_{12} optical phonon. Phonon-assisted luminescence involving other phonons or the paraexciton is at least a factor 30 weaker. Direct recombination is dipole and quadrupole forbidden for the paraexciton and dipole forbidden for the orthoexciton because of the symmetry of the crystal, as was explained in section 2.3. Referring to [27] the lineshape of the spectrum can be analyzed as follows.

In 77 K spectra the sharp direct-recombination line of the orthoexciton can be seen, along with the phonon-emission assisted Stokes line and the phonon-absorption anti-Stokes line, as is shown in figure 2.8. The Stokes line starts at 13.6 meV lower energy than the direct-recombination line and can be observed as a broad emission band. The anti-Stokes line starts at 13.6 meV higher energy. This process requires the presence of phonons, so it can only be observed at elevated temperature. The shape of each of the phonon-assisted lines is given by the kinetic energy distribution

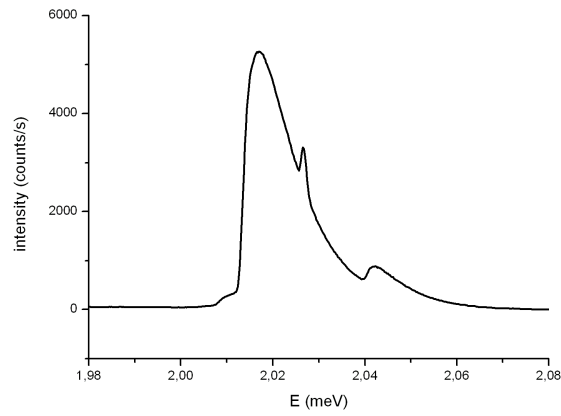


Figure 2.8: Typical luminescence spectrum for Cu_2O at 77 K. The sharp peak in the middle is the direct luminescence. The peak on the left side is the phonon-assisted Stokes luminescence and the peak on the right is the phonon-assisted anti-Stokes luminescence. The phonon involved is the Γ_{12} optical phonon which has an energy of 13.6 meV. The very small peak around 2.01 eV is caused by phonon-assisted luminescence involving the Γ_4 phonon that has an energy of 18.7 meV.

of the excitons [28], since the phonon-assisted luminescence is allowed for all exciton momenta with approximately constant transition probability and the phonon dispersion relation is quite flat. In equilibrium and at low density the energy distribution is the Maxwell-Boltzmann distribution:

$$n(E) \propto (E - E_G)^{1/2} e^{\frac{-E}{k_B T}}. \quad (2.11)$$

Here E_G is the bandgap energy as given by equation 2.9 or 2.10. The relative heights of the Stokes and anti-Stokes band depend on the occupation number of the Γ_{12} optical phonons in the same way as Raman scattering bands

$$I(S)/I(A) = (1 + f)/f = e^{E_{12}/k_B T_{lattice}}. \quad (2.12)$$

Here E_{12} is the phonon energy and f is the Bose-Einstein occupation number.

These formulas do not take into account reabsorption of excitons. Because light with an energy of 13.6 meV above the band bottom can be absorbed by assistance of emission of a Γ_{12} optical phonon, the anti-Stokes phonon emission luminescence is selectively absorbed. This peak will thus be smaller than simple theory predicts. The excitonic temperature determines the width and lineshape of the luminescence and the optical phonon temperature determines the relative heights of the luminescence bands. This allows to extract both temperatures from a single experiment.

When we take into account absorption for an indirect transition two absorption edges will arise. The absorption coefficients are given by

$$\alpha_S(E) = K_S \sqrt{E - E_0 + \hbar\Omega} \quad (2.13)$$

$$\alpha_{AS}(E) = K_{AS} \sqrt{E - E_0 - \hbar\Omega} \quad (2.14)$$

Here $K_S = af$ and $K_{AS} = a(f + 1)$ with a a constant. f is the Bose-Einstein distribution.

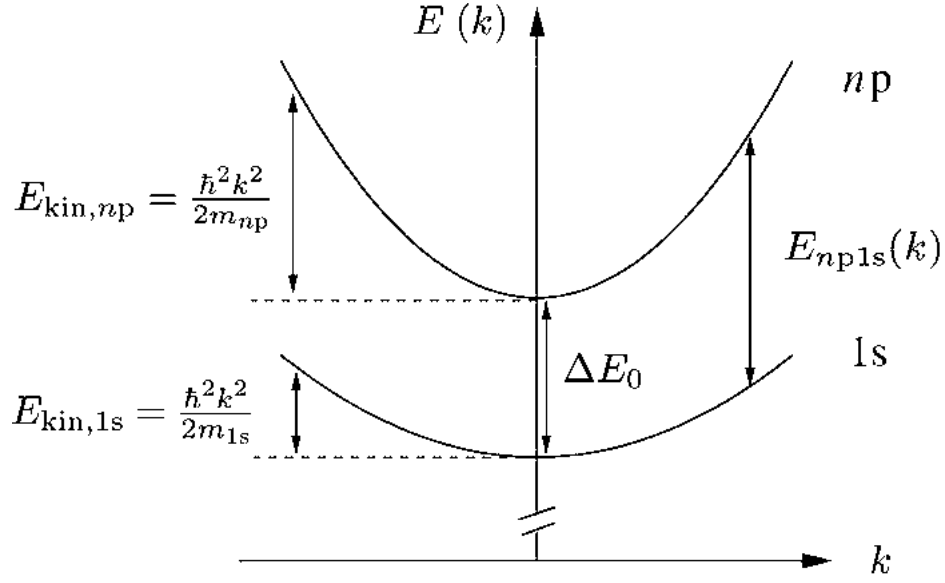


Figure 2.9: Dispersion of generalized 1s and np states including the notations which are used to deduce the theoretical lineshape of induced 1s \rightarrow np absorption. Picture taken from [16].

The total luminescence $F(E)$ is thus given by

$$\begin{aligned}
 F(E) &= F_S(E) \exp(-\alpha_S(E)d) + F_{AS}(E) \exp(-\alpha_{AS}(E)d) \\
 F_S(E) &= \sqrt{E - E_0 + \hbar\Omega} \exp\left(-\frac{E - E_0 + \hbar\Omega}{k_B T}\right) \\
 F_{AS}(E) &= \frac{f}{f+1} \sqrt{E - E_0 - \hbar\Omega} \exp\left(-\frac{E - E_0 - \hbar\Omega}{k_B T}\right)
 \end{aligned} \tag{2.15}$$

Here d is the penetration depth of the light. For calculating $f/(f+1)$ the lattice temperature should be used. The T refers to the exciton gas temperature.

2.7 Induced absorption

When light passes a sample where excitons are present, the transmission will change according to $T^* = T \exp(-\alpha l)$, where T^* is the transmission when excitons are present, T is the transmission when no excitons are present, α is the induced absorption, and l is the thickness of the sample. Neglecting changes in reflection, when calculating differential transmission the reflection term cancels and it follows that

$$-\Delta T/T = \frac{T^* - T}{T} = 1 - \exp(-\alpha l). \quad (2.16)$$

Following [16] we will derive a formula to calculate α . For analyzing the lineshape we can consider two generalized states 1s and np. We assume that the momentum of the photon involved is approximately zero. Since we are dealing with the situation $m_{1s} > m_{np}$ the energy gap between these states increases with increasing k , see figure 2.9:

$$E_{np1s}(k) = \Delta E_0 + \frac{\hbar^2 k^2}{2} \cdot \left(\frac{1}{m_{np}} - \frac{1}{m_{1s}} \right). \quad (2.17)$$

Here ΔE_0 is the energy gap at the point $k = 0$. Disregarding homogeneous broadening, the transition rate W_{np1s} can directly be written by applying Fermi's Golden Rule:

$$W_{np1s} = \frac{2\pi}{\hbar} \int |\mu_i|^2 f_{1s}(k) [1 + f_{np}(k)] f_\gamma(q) \delta [E_{np1s}(k) - \hbar c q] d^3 k \quad (2.18)$$

where μ_i is the transition matrix element and f_{1s} , F_{np} and f_γ are the distribution functions of the 1s excitons, np excitons and infrared photons, respectively. From this equation we can derive the lineshape of the induced absorption assuming:

1. The matrix element μ_i is k -independent,

2. Since dipole transitions in a cubic lattice are direction independent it follows

$$d^3k = 4\pi k^2 dk,$$

3. The population of the np level can be neglected.

This approach yields

$$\alpha(E) \propto \int k^2 f_{1s}(k) \delta [E_{np1s}(k) - E] dk \quad (2.19)$$

where $E = \hbar c |q|$ is the energy of the infrared probe beam. By using equation 2.17 this equation can be transferred into an integral over E_{np1s} :

$$\alpha(E) \propto \int f_{1s}(E_{np1s}) \sqrt{E_{np1s} - \Delta E_0} \delta (E_{np1s} - E) dE_{np1s}. \quad (2.20)$$

We use the Boltzmann approximation for a thermal distribution within the 1s band, which leads to

$$\alpha = A \sqrt{E - \Delta E} \exp \left(- \frac{E - \Delta E}{\left(\frac{m_s}{m_p} - 1 \right) k_b T} \right). \quad (2.21)$$

Here A is a constant, ΔE is the energy difference between the exciton levels, m_s is the exciton mass of the 1s level, m_p is the exciton mass of the 1p level, and k_b is Boltzmann's constant. Finally the line broadening due to temperature is taken into account by convoluting α with the function $\frac{\Gamma}{\Gamma^2 + E^2}$. Here Γ is the full width at half maximum (FWHM) of the measured curve.

For the fitting we have to take into account interference effects when the surfaces of the crystal are parallel. More precisely, the distance between the surfaces should not differ more than the wavelength of the light. The reason for this is that just like in a Fabry-Pérot etalon multiple internal reflections can occur. Following [29] we calculate the transmission with

$$T = |t|^2 = \left| \frac{4\tilde{n} \exp \left(\frac{\omega(in-k)l}{c} \right)}{(1 + \tilde{n})^2 - (1 - \tilde{n})^2 \exp \frac{2\omega(in-k)l}{c}} \right|^2 \quad (2.22)$$

$$\begin{aligned}\omega &= E/\hbar \\ \tilde{n} &= n + ik\end{aligned}$$

Here n is the real part of the refractive index and k is the imaginary part. l is the sample thickness. When excitons are excited, the imaginary part of the refractive index will change according to $\tilde{n} = n + ik \rightarrow n + i(k + k^*)$, where

$$\begin{aligned}k^* &= \frac{c}{2\omega} \alpha_{1s \rightarrow np} \\ &\propto \frac{1}{\omega} \int \sqrt{E - E' - \Delta E} \exp \left[-\frac{E - E' - \Delta E}{\left(\frac{m_s}{m_p} - 1\right) k_b T} \right] \frac{\Gamma/2}{E'^2 + (\Gamma/2)^2} dE' \quad (2.23)\end{aligned}$$

For calculating n a Sellmeier equation was used based on previous work of the University of Tokyo (private communication). Changes in n are neglected. By inserting the changed \tilde{n} in the formula for the transmission, we can calculate T^* , the transmission when excitons are absorbed. Finally we calculate the differential transmission $DTS = -\Delta T/T = -(T^* - T)/T$.

2.8 Exciton density

By calculating the Einstein coefficients and the dielectric function and relating these to the oscillator strength, it can be shown that the oscillator strength is given by

$$f_i = \frac{2m\Delta E}{\hbar^2 e^2} |\mu_i|^2 \quad (2.24)$$

where m is the reduced mass, μ_i the dipole matrix element and ΔE is the transition energy. From the dielectric function with simultaneous cw laser excitation $\epsilon(E) = \tilde{\epsilon}(E) + \sum_i \chi_i(E)$ we take the additional imaginary part $\tilde{\epsilon}_2$, because this determines the induced absorption [16]:

$$\tilde{\epsilon}_2 = \text{Im} [\epsilon(E) - \tilde{\epsilon}(E)] = \text{Im} \left(\sum_i \chi_i \right) \quad (2.25)$$

$$\chi_i(E) = \frac{n_{1s}\hbar^2 e^2}{m\epsilon_0} \frac{f_i}{\Delta E^2 - E^2 - i\hbar\Gamma E} \quad (2.26)$$

where Γ is the damping and n_{1s} is the density of the 1s ortho or para excitons, depending on the transition type. Now the induced absorption can be written as

$$\alpha_{ind,i}(E) = \frac{\tilde{\epsilon}_{2,i}(E)E}{\hbar c n(E)} \approx \frac{Im[\chi_i(E)]E}{\hbar c \sqrt{\epsilon_B}} = \frac{2E_i n_{1s} |\mu_i|^2}{\hbar \sqrt{\epsilon_B} \epsilon_0 c} \frac{\hbar\Gamma/4}{(\Delta E - E)^2 + (\hbar\Gamma/2)^2}. \quad (2.27)$$

Here c is the velocity of light. The index of refraction is approximated by $\sqrt{\epsilon_B}$. The last equation is obtained by inserting equation 2.24 and 2.26 for $\hbar\Gamma \ll \Delta E$. The ratio on the right hand side describes a normalized Lorentzian with an integrated area of $\pi/2$. Integration of equation 2.27 yields the connection between the density of the 1s exciton and the area of induced absorption

$$n_{1s} = \frac{\hbar\epsilon_0 c \sqrt{\epsilon_B} A_i}{\pi |\mu_i|^2 \Delta E} \quad \text{with } A_i = \int \alpha_{ind,i}(E) dE \quad (2.28)$$

Because the Bohr radius in Cu_2O is different from the hydrogen atom, also the dipole matrix element will be different. Also, the Bohr radii for the 1s and np levels are not equal. The np levels all have the same Bohr radius of ≈ 1.1 nm, which can be deduced from their Rydberg energy and reduced mass. For the 1s exciton the enhanced binding energy leads to a smaller value of the Bohr radius of ≈ 0.53 nm. Since the dipole matrix element does not act on spin, the matrix element for para and orthoexcitons between the same levels has the same value. Taking into account the different Bohr radii, the values are calculated as follows [16]:

transition	$\mu_{np1s,z}$ (H-atom)	$\mu_{np1s,z}$ (yellow series exciton)
1s - 2p	$\frac{2^{15/2}}{3^5} a_b e$	$\frac{2^{15/2} a_{b,1s}^{7/2} a_{b,np}^{5/2}}{(2a_{b,np} + a_{b,1s})^5} e \approx 2.6 \cdot 10^{-29} Cm$
1s - 3p	$\frac{3^3}{2^{13/2} a_b e}$	$\frac{2(a_{b,1s} a_{b,np})^{7/2} - a_{b,1s}^{9/2} a_{b,np}^{5/2}}{(a_{b,1s} + 3a_{b,np})^6} 2^{-11/2} 3^3 e \approx 1.4 \cdot 10^{-29} Cm$

Chapter 3

Experimental setup

3.1 Visible pump - infrared probe measurements

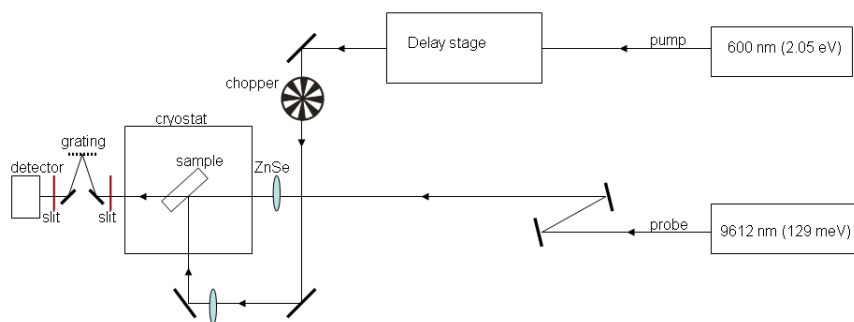


Figure 3.1: Experimental setup for the pump-probe measurements. For a description, see text.

The experimental setup is shown in figure 3.1. All experiments are done at 6 or 8 K. We excite the sample with a 800 nm or 600 nm pulse which has a width of 120 fs. The repetition rate is 1 khz. This pulse is produced as follows. A continuous wave diode-pumped 532 nm laser (Millennia) is used as a pump for the modelocked Ti:sapphire laser. This two-laser system (MaiTai) produces pulses of

80 fs with a repetition rate of 80 MHz. Chirped pulse amplification is used to reduce the brightness of the beam, because bright beams have the tendency to focus destructively. Initially a very short pulse duration is generated and the pulse is stretched afterwards. The low-brightness pulse is amplified by a factor of up to 10^6 . The amplification takes place as the optical pulse passes through a Ti:sapphire laser rod, which has been optically excited by a laser pulse from a 523.5 nm Nd:YLF laser (Evolution). The regenerative amplification technique enables the pulse to multipass the rod, resulting in a high overall gain.

The 800 nm beam that comes out of the laser system (called Hurricane (Spectrophysics)) is split in two beams equal in intensity of which the pulses have a pulse power of 300-400 mW. If we need a pump beam with a wavelength of 600 nm, both are fed into a LBO (lithium triborate) crystal based ultrashort pulse 5-pass parametric frequency convertor (TOPAS). For the pump beam, optical parametric amplification and second harmonic generation is used to make 600 nm pulses out of the 800 nm input pulses. For the probe beam, optical parametric amplification and difference frequency generation are used to produce an output beam with a frequency in the infrared (IR). If we need a 800 nm pump, the pulses that leave the Hurricane system are used directly and only one beam is fed into the TOPAS system. TOPAS has five amplifying stages. The first one serves as a seeder emitting broad-banded superfluorescence. In the second preamplifiers shape the beam. The third pass through the nonlinear crystal usually has a negligible amplification. The fourth one amplifies the beam a bit. The last amplification stage boosts the energy of the parametric pulse. The divergence of the beam is close to the diffraction limit. The maximal efficiency of the process is 30 %.

Hereafter the pump beam goes to the delay stage, which can be moved by a stepper motor to set the delay between the probe and the pump beam to the desired value. A chopper with a frequency of 333 Hz is used to modulate the pump beam.

For the probe beam, a ZnSe lens is used to focus the beam on the sample, because quartz absorbs almost all IR. The pump beam creates excitons in the Cu_2O sample by a one-photon (600 nm light) or two-photon (800 nm light) absorption process. The excitons in the 1s-ortho level, after the extra energy is dissipated. Paraexcitons are created by down-conversion from the orthoexciton level. The probe beam then excites the 1s ortho and 1s paraexcitons to exciton levels which lie higher in energy. With the probe energy used we can make 1s-2p para and 1s-3p ortho transitions. The detection system consists of a monochromator, a nitrogen cooled InSe detector and a lock-in amplifier (Stanford research). The lock-in amplifier measures the difference in absorption between the situation when the pump beam is present and creates excitons, and when the pump beam is absent.

3.2 Time-resolved luminescence

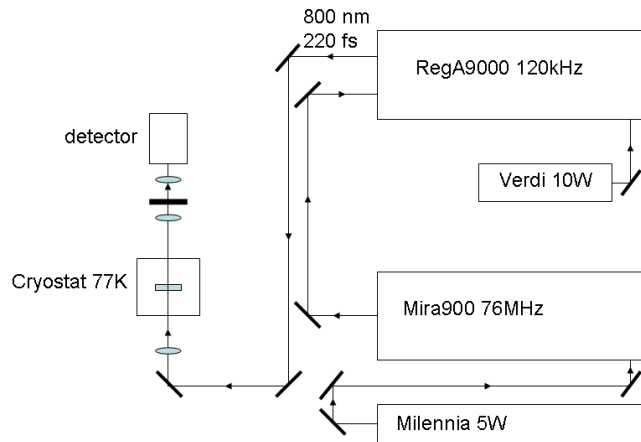


Figure 3.2: The experimental setup for measuring luminescence. For a description, see text.

The experimental setup is shown in figure 3.2. All measurements are done at

77 K. At this temperature para-to-ortho upconversion is efficient enough to see luminescence from paraexcitons that decay via the orthoexciton state to the ground state. The upconversion process depends on temperature as $\exp(-\Delta E/k_b T)$, which means that it is about 10^8 times as large at 77 K compared to 4 K. We excite the sample with a 800 nm pulse which has a width of 220 fs. The repetition rate is 120 kHz. This pulse is produced as follows. A continuous wave argon ion laser (Millennia) with operating power 5 W at 514 nm is used as a pump for the modelocked ultrafast Mira 900 laser. The technique used to modelock the Mira laser is Kerr Lens Modelocking. The optical cavity is specifically designed to utilize changes in the spatial profile of the beam produced by self-focusing from the optical Kerr effect in the Ti:sapphire crystal, which is used as the gain medium. This self-focusing results in higher round trip gain in the modelocked than in the CW operation due to an increased overlap between the pumped gain profile and the circulating cavity mode. In addition, an aperture is placed at some position within the cavity to produce lower round trip loss in the modelocked than in the CW operation. Group velocity dispersion compensation is used to produce pulses of approximately 200 femtoseconds at a repetition rate of 76 MHz.

The light of the Mira laser is fed into a compact regenerative amplifier system (RegA 9000) for increasing the pulse energy. For this a green cw laser (Verdi) operated at 10 W is used as a pump source. Beam tubes enclose the laser path and prevent mirror contamination and dust in the path of the beam. The input beam from the Mira laser passes through a Faraday isolator and a single pulse is injected into the RegA by a TeO_2 acousto-optic cavity dumper. In 20 to 30 round trips the pulse is expanded to 30 ps length and amplified. The cavity dumper then extracts a single pulse of several μJ energy. Finally this pulse returns through the Faraday isolator and is separated from the input beam path by a polarizer.

The pump power can be varied, but is usually around 10 mW. The energy density

is in the order of $700 \mu\text{J}/\text{cm}^2$ for a spotsize with a FWHM of $115 \pm 2 \mu\text{m}$. With a lens ($f = 10 \text{ cm}$) the beam is focused onto the sample. The sample is placed in a cryostat with a temperature of 77 K. The sample holder consists of a front plate with a small hole of 0.5 mm radius and a back plate with a hole of 2 mm radius. In between the plates the sample is placed. The transmitted beam is made parallel with another lens ($f = 10 \text{ cm}$) and focused into the detector with a third lens ($f = 10 \text{ cm}$).

For the luminescence versus wavelength measurement we detect the signal with a triple grating monochromator (acton Research corporation, spectrapro-275) and a CCD-camera, which is Peltier cooled to -70 degrees Celcius. A low-pass filter is inserted to prevent the laser light from reaching the detector. The slitwidth is $100 \mu\text{m}$, which corresponds to a theoretical resolution of 0.24 nm for the 1200 grooves/mm grating and 1.92 nm for the 150 grooves/mm grating. The resolution was measured to be 2 nm for the 150 grooves/mm grating, which is only slightly lower. For the lifetime measurement the light falls into a photomultiplier (R 636-10, Hamamatsu). A filter (XB106, Omega optical) cuts all the wavelengths except for the range 605 to 615 nm. We record the voltage versus time decay curve, averaged over a few hundred pulses, with a digitizing oscilloscope (Tektronix TDS 744A).

The vacancy spectrum measurement is done with a green Nd:YVO₄ laser (Northrop Grumman) with 532 nm wavelength and 2 mW laser power. A 800 nm beam is used to excite the Nd:YVO₄ crystal. The crystal then will excite 1064 nm light, which is converted into 532 nm with a second harmonic crystal. The spot is focussed on the hole in the back plate of the sample holder, which has a radius of 2 mm. The luminescence spectra have been recorded in a back scattering geometry using the same monochromator and CCD-camera as used for the 800 nm luminescence measurements. A longpass filter (cutting wavelength 560 nm) is inserted to cut the 532 nm peak from the spectrum.

3.3 CW spectroscopy

3.3.1 Description of the setup

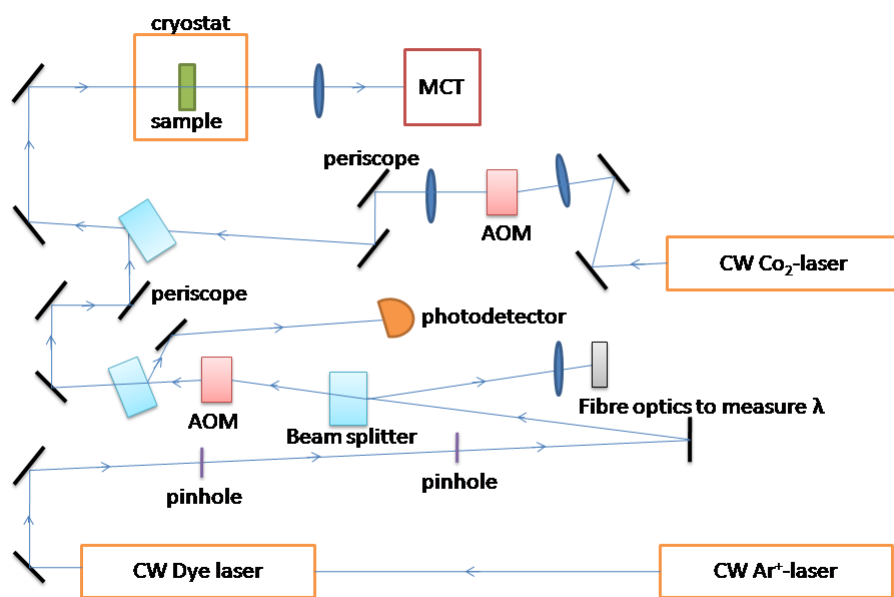


Figure 3.3: The experimental setup for the CW Lyman spectroscopy measurements. For an explanation of the different parts, see text.

The experimental setup is shown in figure 3.3. As a pump beam a 605 nm pulse with a repetition rate of 5 kHz is used. A CW Ar⁺-laser (Innova 200, 20W) is used as a pump source for a dye ring laser (Coherent 899-21), which can produce every desired wavelength between 570 and 630 nm. A liquid solution of rhodamine is used as a gain medium. A dye jet keeps the dye flowing to avoid degradation under the influence of light. The output power used is typically 20-50 mW. A beamsplitter splits the output beam. One beam goes to fibre optics to measure the output

wavelength. The other beam goes to an AOM (acousto-optic modulator). An AOM consists of a piezoelectric transducer which creates sound waves with a frequency of 40 MHz in a material like glass or quartz. These can be thought of as moving periodic planes of expansion and compression that change the index of refraction, which causes diffraction into several orders. Here the CW beam is converted to a pulse with a frequency of 5 kHz and a pulsewidth of 100 μ s by turning the AOM on and off with this frequency. Another beam splitter splits the output beam. One beam goes to a photodetector which is used to measure the laser power and acts as a negative feedback circuit to stabilize the output of the AOM. The other beam passes a periscope to change the distance between the beam and the table and falls into another beam splitter which merges it with the probe beam.

The probe beam is produced by a tunable single line CW CO₂-laser (LCD-1A molecular laser). Population inversion is achieved by exciting the carbon dioxide with high power radio waves. From the excited state the molecule will decay to one of two excited states with lower energy. Because both of these states have different rotational levels, photons with different, but quite close energies are released. 18 Different wavelengths can be produced, which are listed in table 3.3.1. The desired wavelength can be selected by setting a grating to the correct orientation. From the two excited states the carbon dioxide molecule will decay to the groundstate non-radiatively. The output beam goes to a germanium AOM, again driven at 40 MHz. Both AOM's are driven by a pulse generator (wavefactory WF1946), with which also the delay between the pulses can be set. The output pulse has a pulsewidth of 50 μ s and a repetition rate of 10 kHz. The output power is 5 W but is reduced to 100 μ W with a neutral density filter for this experiment. A periscope changes the height of the beam. Afterwards the pulses are merged with the pump beam by a beam splitter. Both pump and probe beam are focused by an off-axis parabolic mirror onto the sample which is placed in a He dynamic flow cryostat with a minimum

temperature of 4 K. In front of the sample an aperture mask with a diameter of 200 μm is placed to ensure spatial overlap between the pump and probe beam. The transmitted probe signal is focused with a lens and detected by a MCT-detector (mercury(II) cadmium(II) telluride, KMPV 50-0.5-J2, Kolmar)). It is cooled with liquid nitrogen to reduce noise due to thermally excited current carriers.

λ (μm)	energy (meV)	λ (μm)	energy (meV)	λ (μm)	energy (meV)
9.45805	131.21096	9.55243	129.91462	9.65742	128.50229
9.47306	131.00308	9.56918	129.6872	9.67507	128.26781
9.48835	130.79192	9.58823	129.42957	9.69483	128.00637
9.50394	130.57748	9.60357	129.22274	9.714	127.7538
9.51981	130.35977	9.62122	128.98574	9.73347	127.49817
9.53597	130.13882	9.63917	128.74558	9.75326	127.23952

Table 3.1: The single line CO₂-laser can be tuned to 18 different wavelengths.

The signal from the MCT detector is sent into two lock-in amplifiers. The waveform of the amplitude modulation applied is a 50 % duty ratio square wave. The repetition frequency is 5 kHz for the pump beam and 10 kHz for the probe beam. The paraexciton gas reaches a steady-state regime on a much shorter timescale. The intensity of the probe beam is monitored as the 10 kHz component ($V(10kHz)$) of the lock-in amplifier and the 1s-2p induced absorption of paraexcitons appears as the 5 kHz component ($V(5kHz)$). The negative differential transmission is calculated using equation 3.12 (see next section). This procedure is repeated for each probe wavelength. The minimum transmission change that can be measured is about $3 \times$

10^{-5} and is limited by the observation bandwidth and the dynamic reserve of the lock-in amplifier.

For the lifetime measurement we fix the probe wavelength at $9.47306 \mu\text{m}$ (131 meV). The delay between the pump AOM-pulse and the probe AOM-pulse is varied between 0 and $2.3 \mu\text{s}$. The pulsewidths are now $3 \mu\text{s}$ for the pump and 70 ns for the probe. For every delay we measure D , the ratio of $(V(5\text{kHz}))$ over $(V(10\text{kHz}))$, averaged over 100.000 points. From this the differential transmission can be calculated (see next section). A preamplifier is used to cut the DC-200 Hz frequencies and to amplify the signal 20 times. After this an AD-converter (DL750 scopecoder, Yokogawa) converts it to a digital signal. A temperature of 77 K is used. The reason for this is that we want to limit the diffusion, because it makes analysis of the spectrum complicated. The diffusion coefficient is limited by the exciton-phonon interaction, which is larger at higher T, because more phonons are present. This means that the higher the temperature, the smaller the diffusion will be.

3.3.2 Probe and pump pulse modulation

For CW spectroscopy the pump pulse has a frequency of 5 kHz and the probe has a frequency of 10 kHz. We assume that both AOM's produce block pulses. This means that only one of every two probe pulses is modulated by the exciton gas created by the pump beam. This is shown in figure 3.4. If we define the height of the unmodulated probe pulse as A and the height of the modulated pump pulse as Ax , the differential transmission (DTS) is given by

$$DTS = \frac{A - Ax}{A} = 1 - x \quad (3.1)$$

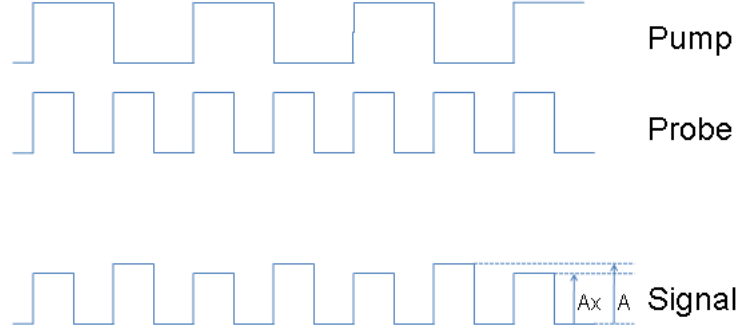


Figure 3.4: Pump and probe modulation. The pump pulse has a frequency of 5 kHz and the probe pulse has a frequency of 10 kHz.

The pulse signal $f(t)$ is periodic with a period consisting of 4 parts:

$$f(t) = \begin{cases} A & (0 \leq t < \tau) \\ 0 & (\tau \leq t < 2\tau) \\ Ax & (2\tau \leq t < 3\tau) \\ 0 & (3\tau \leq t < 4\tau) \end{cases} \quad (3.2)$$

We expand this signal in a fourier series

$$\begin{aligned} f(t) &= \frac{a_0}{2} + \sum_{n=1}^{\infty} \left(a_n \cos \frac{n\pi}{2\tau} t + b_n \sin \frac{n\pi}{2\tau} t \right) \\ a_n &= \frac{1}{2\tau} \int_0^{4\tau} f(t) \cos \frac{n\pi}{2\tau} t dt \\ b_n &= \frac{1}{2\tau} \int_0^{4\tau} f(t) \sin \frac{n\pi}{2\tau} t dt \end{aligned} \quad (3.3)$$

When we calculate the coefficient for each component we get [29]:

$$\begin{aligned} a_0 &= \frac{1}{2\tau} \left(\int_0^{\tau} A dt + \int_{2\tau}^{3\tau} Ax dt \right) \\ &= \frac{A(1+x)}{2} \end{aligned} \quad (3.4)$$

$$a_n = \frac{1}{2\tau} \left(\int_0^\tau A \cos \frac{n\pi}{2\tau} t dt + \int_{2\tau}^{3\tau} A x \cos \frac{n\pi}{2\tau} dt \right) \quad (3.5)$$

$$= \frac{A}{n\pi} \left(\sin \frac{n\pi}{2} + x \sin \frac{3n\pi}{2} \right)$$

$$b_n = \frac{1}{2\tau} \left(\int_0^\tau A \sin \frac{n\pi}{2\tau} t dt + \int_{2\tau}^{3\tau} A x \sin \frac{n\pi}{2\tau} dt \right) \quad (3.6)$$

$$= \frac{A}{n\pi} \left[\left(1 - \cos \frac{n\pi}{2} \right) + x \left(\cos n\pi - \cos \frac{3n\pi}{2} \right) \right].$$

(3.7)

Substituting these coefficients in the fourier series formulas then gives

$$\begin{aligned} f(t) &= A \left(\frac{1+x}{4} + \frac{1-x}{\pi} \cos \omega t + \frac{1-x}{\pi} \sin \omega t + \frac{1+x}{\pi} \sin 2\omega t + \dots \right) \quad (3.8) \\ &= A \left(\frac{1+x}{4} + \sqrt{2} \frac{1-x}{\pi} \sin \left(\omega t + \frac{\pi}{4} \right) + \frac{1+x}{\pi} \sin 2\omega t + \dots \right) \end{aligned}$$

where $\omega = \frac{\pi}{2\tau}$. With the lock-in amplifier we pick up the ω and 2ω component, of which the magnitudes are given by

$$\omega \text{ component} \dots \sqrt{2} A \frac{1-x}{\pi} \quad (3.9)$$

$$2\omega \text{ component} \dots A \frac{1+x}{\pi} \quad (3.10)$$

The signal we measure is the division D of the 5 kHz component over the 10 kHz component

$$D = \frac{\omega \text{ component}}{2\omega \text{ component}} = \frac{\sqrt{2}(1-x)}{1+x} \quad (3.11)$$

We can see from the definition of DTS , eqn 3.1 and eqn 3.11 that it can be related to D as

$$DTS = \frac{2D}{\sqrt{2} + D}. \quad (3.12)$$

Furthermore, we see that there is a phase shift of $\frac{\pi}{4}$ between the ω and 2ω component.

Chapter 4

Results and discussion

In this chapter some results of the experiments will be shown and discussed. We measured few samples in Groningen and Tokyo. The properties of the samples are listed in table 4.1. The luminescence, differential transmission, lifetime and vacancy concentration of the different samples will be compared.

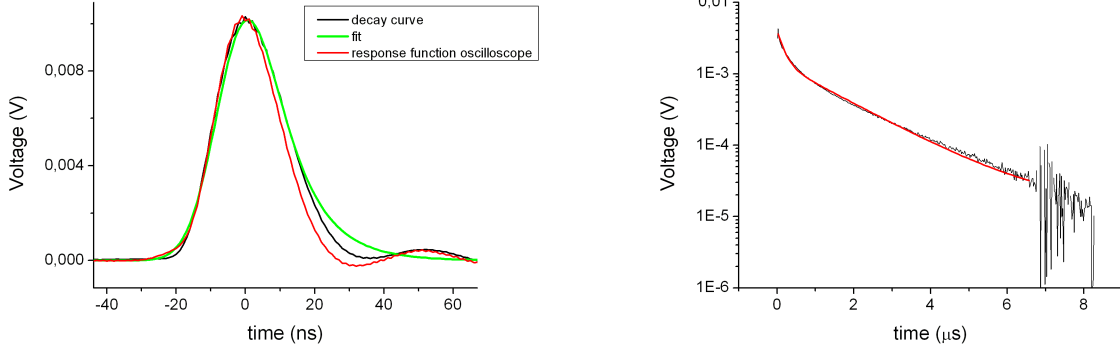
4.1 Lifetime

In figure 4.1 the decay of the luminescence in time of two samples is shown. The measurements are done at 77 K. This means that we can probe the paraexcitons, because the amount of paraexcitons that have enough thermal energy to be upconverted to the orthoexciton level is large enough. For sample C we find a lifetime of around 10 ns. Because the lifetime is very short, we have to take into account the response function of the detection system for the fitting. This is done by first fitting the left side of the curve with a gaussian and afterwards convoluting the decay

sample	thickness (μm)	orientation	measured lifetime	city	remarks
A	140	(110)	14 ± 3 ns	Groningen	grown in Paris
B	765	(110)	12 ± 3 ns	Groningen	grown in Paris
C	360	(110)	10 ± 3 ns	Groningen	grown in Paris
D	375	(100)	5 ± 5 ns	Groningen	grown in Paris
E	220	unknown	1.7 ± 0.2 μs	Tokyo	
F	220	(100)	1.2 ± 0.2 μs	Tokyo	
G	≈ 1000	unknown	1.5 ± 0.2 μs	Tokyo	
H	≈ 2500	(100)	1.8 ± 0.2 μs	Tokyo	surfaces not parallel
I	960	(110)	2.4 ± 0.2 μs	Tokyo	
J	400	unknown	1.5 ± 0.2 μs	Tokyo	
K	500	(100)	not measured	Groningen	grown in Paris

Table 4.1: For the experiments in Tokyo 10 different samples were used. Sample K was measured in Groningen. In this table some properties of these samples are listed.

function with this gaussian. For samples with a lifetime in the order of μs fitting is done with a two-exponential decay. The fast decay in the beginning of the curve of sample G is due to two-body collision. The timescale found for this two-body decay is between 100 and 300 ns. The slow decay is due to free paraexciton decay. Since the interval between pulses is less than 10 μs , the measured time interval is too short for the decay of excitons bound to impurities to be seen. For sample G we found a free exciton lifetime of 1.5 μs . Because this is a much longer timescale than for the samples with a short lifetime, we do not take the response function of the detection system into account. The noise at later times is probably caused by crosstalk between the signal and the trigger of the oscilloscope, or by acousto-optical



(a) Short lifetime decay spectrum for sample C. Incident power: 25 mW, energy density 20 mJ/cm², sample thickness 360 μm.

(b) Long lifetime decay spectrum for sample G. Incident power: 2 mW, energy density 1.6 mJ/cm², sample thickness 1 mm. Averaged over 10 decay curves.

Figure 4.1: Different decay spectra. Measurements were done in the time-resolved luminescence setup at 77 K. The excitation wavelength was 800 nm.

modulation of the laser, since the laser frequency is used as trigger signal. When we measured the response function of the detection system, we saw noise at exactly the same position, which shows that this noise is extrinsic. When laser power was varied, no change in lineshape was observed. This indicates that we are in the linear part of the curve shown in figure 4.4.

With the CW setup also the lifetime of sample I was measured. The decay curve is shown in figure 4.2. With this setup we could measure the decay curve with a very good signal-to-noise ratio of about 1×10^{-5} . Fitting was done with a two exponential decay [30]: $\Delta\alpha(t) = A_f \exp(-t/\tau_f) + A_b \exp(-t/\tau_b)$, where $\Delta\alpha$ is the induced absorption coefficient, $A_{f(b)}$ is the signal amplitude due to free (bound) excitons, and $\tau_{f(b)}$ is the lifetime of free (bound) excitons. A bound exciton means in this case that it is caught by a vacancy. Because of the noise at the beginning of the curve, we cannot see the fast two-body decay. Unfortunately the lifetime

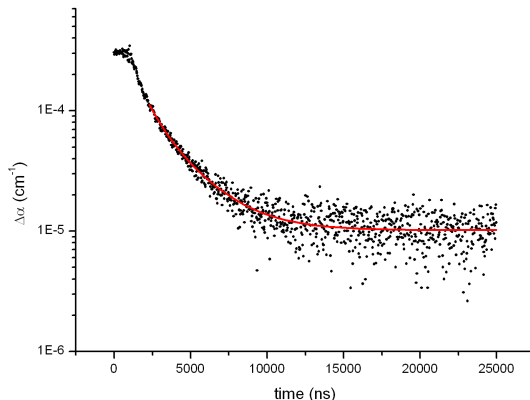
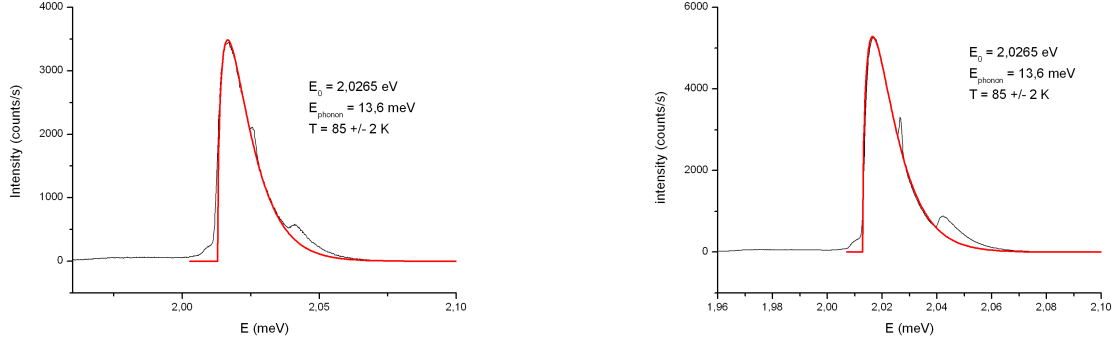


Figure 4.2: Decay curve for sample I measured with the CW setup. Incident power: 2 mW, energy density $\approx 300 \mu\text{J}/\text{cm}^2$, temperature 77 K and sample thickness 960 μm .

found depends on the fitting interval. This means that we cannot neglect diffusion. Since developing a model to take diffusion into account is complicated and time consuming, we estimate the lifetime of the excitons by fitting at later times, when diffusion is assumed to be smaller than at early times. A lifetime of 800 ± 200 ns is found for free excitons and 2500 ± 160 ns for bound excitons. The value for free excitons is three times as small as the lifetime of 2400 ± 100 ns found in the time-resolved luminescence setup. Thus, also at later times diffusion cannot be neglected and we can only take the extracted lifetimes as a minimum value.

We see an two orders of magnitude difference between lifetimes of different samples. In the next sections luminescence, induced absorption and vacancy concentration will be compared for samples with a short lifetime and a long lifetime. Differences found can be an explanation for the difference in lifetime.

4.2 Luminescence



(a) Short lifetime luminescence spectrum for sample D. Incident power: 25 mW, energy density 20 mJ/cm², sample thickness 375 μm .

(b) Long lifetime luminescence spectrum for sample E. Incident power: 2 mW, energy density 1.6 mJ/cm², sample thickness 220 μm .

Figure 4.3: Different luminescence spectra. Measurements were done in the time-resolved luminescence setup at 77 K. We used a slit with 1200 grooves/mm. The excitation wavelength was 800 nm.

In figure 4.3 two typical luminescence spectra are shown. The measurements were done at 77 K with an excitation wavelength of 800 nm. The left one is for sample D with a lifetime in the order of ns. The right one is for sample E with a lifetime in the order of μs . The fitting was done with a simplified form of formula 2.15. We want to extract the exciton temperature from these measurements, which can be done by only fitting the Stokes phonon-assisted luminescence peak. For both samples we find an exciton temperature of about 85 K. For all samples measured except one the exciton temperature was 80-85 K. Only sample H had an exciton temperature of 77 K, equal to the lattice temperature. This was a sample of 2.5 mm thickness, at least 2.5 times thicker than the other samples. Probably the larger volume of the sample allows for the exciton gas to cool down more easily. A better fit

on the left side of the curve can be obtained if we take the Γ^4 phonon into account. This is not done in this analysis, because it does not influence the extracted exciton temperature. Also it does not give any extra information about excitons.

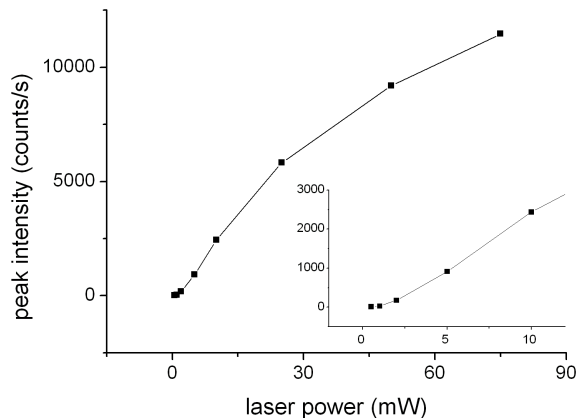


Figure 4.4: Luminescence intensity as a function of laser power measured for sample C. The excitation was done with 800 nm light, which means that two-photon absorption occurs. The inset shows the beginning of the curve, where the intensity is quadratic with the laser power. For laser powers higher than 10 mW (≈ 8 mJ/cm²) saturation starts to be visible.

Something else which was observed is that there is no change in lineshape when the incident power is varied. The peak intensity is quadratic with laser power for low powers. This can be seen in figure 4.4. We expect it to be quadratic, because two photons are absorbed. But this is only seen for very low excitation powers. We already observe saturation effects for powers higher than 10 mW. A striking difference between the low lifetime luminescence curves and the long lifetime ones, is the difference in the luminescence strength when compared for equal incident powers. For the long lifetime samples the luminescence peak intensity was 10-50 times higher for the measurements in reflection geometry and 10-100 times higher

for the measurements in transmission geometry. This will be discussed in section 4.4.

4.3 Differential transmission

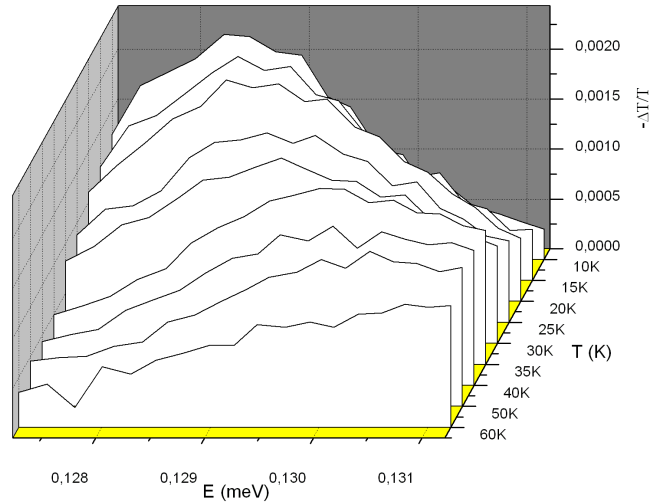


Figure 4.5: Differential transmission spectrum for the 1s - 2p para and 1s - 3p ortho transition for sample H as a function of temperature. The energy density was $2.5 \mu\text{J}/\text{cm}^2$, the excitation wavelength 605 nm, and the sample thickness about 2.5 mm. Since the surfaces of the sample are not parallel, we do not have to take into account interference effects.

Two ways of creating excitons are possible. When doing one-photon absorption, the absorbed photon has an energy only slightly higher than the 1s-orthoexciton level, so orthoexcitons can be created directly. Because of the small penetration depth of the light (about $100 \mu\text{m}$) excitons are mainly created near the surface of the sample. When doing two-photon absorption, the energy of the two photons is high enough to excite excitons in the blue series. After releasing the extra energy

to the lattice, also by this process 1s-orthoexcitons can be created. Both processes can also create paraexcitons by ortho-to-paraexciton downconversion. The 800 nm light has a large penetration depth ($> 500 \mu\text{m}$, [8]), so the excitons are distributed uniformly throughout the sample.

In the CW setup we measured the differential transmission of sample H with a long lifetime and of sample B with a short lifetime. The spectrum for the long lifetime is shown in figure 4.5. Fitting is done as follows using equation 2.16 with α from equation 2.21. There are three fitting parameters: amplitude, mass ratio m_s/m_p , and Γ . T is assumed to be equal to the lattice temperature, because we create a very low density of excitons, about $6\text{-}8 \times 10^{13}/\text{cm}^3$. ΔE can be determined from figure 2.7. Because we can only measure 18 point, we should the parameters found consider as a rough estimate. We find a mass ratio which varies between 1.22 and 1.41, which means a m_p of 1.9-2.2 m_0 , which is slightly higher than the value of 1.86 m_0 found in [16]. As expected from equation 2.21, we see an increase of Γ with increasing temperature. All fitting parameters found are listed in appendix C.

The spectrum for the short lifetime sample B at 10 K is shown in figure 4.6. Spectra were taken for 5, 10, 15, 20, and 25 K. The other spectra can be found in appendix C. The error was calculated by taking the absolute deviation from the mean background value of the probe pulse. This was averaged over two measured background spectra. Fitting was done using equation 2.23.

Because of the short lifetime the signal is quite small, which leads to a large error in the measurements. From fitting we can determine the exciton temperature, FWHM, mass ratio and k^* . These values are not very reliable because of this large error and the fact that we can only measure 18 points. Therefore it is better to see the fit as a simulation which shows how the experimental curve should approximately look like. We find an exciton temperature that is 10-15 K higher than the lattice temperature. For the mass ratio we find a value of about 1.24, which is in agreement

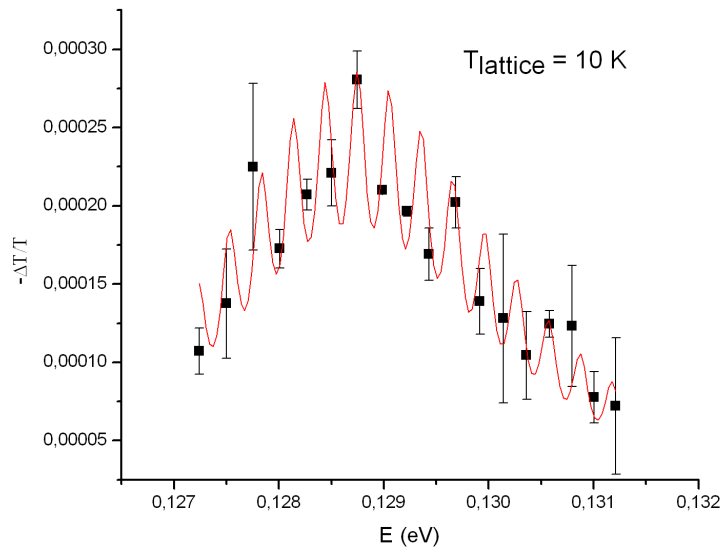


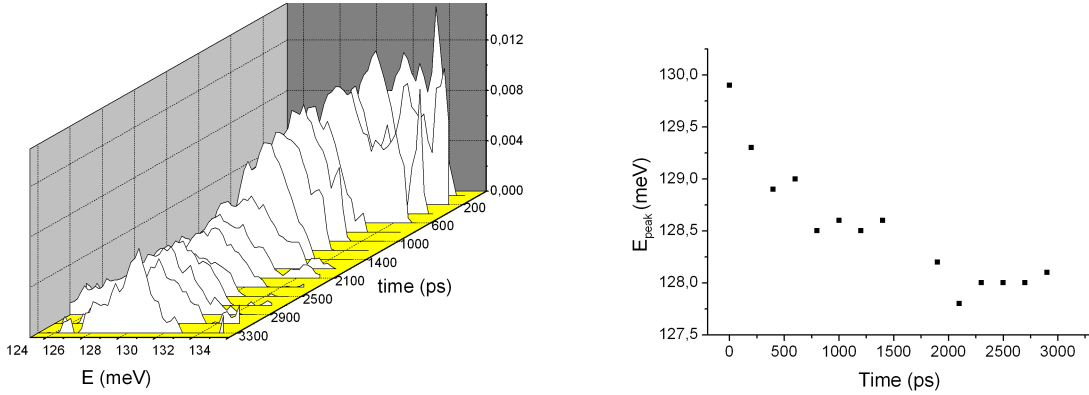
Figure 4.6: Differential transmission spectrum for sample B for $T = 10$ K. The incident power was 45 mW, which corresponds to an energy density of 6.3 mJ/cm^2 , the excitation wavelength was 605 nm, and the sample thickness was $760 \mu\text{m}$.

with the measurements on the long lifetime sample. For the density we find a value in the order of $1-3 \times 10^{13}/\text{cm}^3$, which is approximately five times smaller than for the long lifetime sample. This is surprising, since the excitation power for the short lifetime sample is about 2500 times as high, but the exciton lifetime is about 500 times as small. So we would expect the exciton density to be higher by about a factor of five for the short lifetime sample.

In the CW setup we use 605 nm light for excitation, so the density of excitons created is not constant through our sample, because of the small penetration depth of the light, which is in the order of 100 μm [8]. Using 605 nm light is a compromise between having enough energy for one-photon excitation and a large penetration depth. Fortunately, it can be shown that assuming an induced absorption independent of the position in the sample gives the mean exciton density. This means we can just use equation 2.28 for the calculation. This is also intuitively clear, because the positions in the sample where excitons are created do not make a difference for the calculation of the mean density.

In the visible pump - infrared probe setup we measured differential transmission spectra as a function of time. We could measure in the time interval from 0 to 3.6 ns. Here we used a sample with a thickness of 500 μm (sample K). In figure 4.7 a typical spectrum is shown. The inset shows how the peak energy shift as a function of time. The reason for this is the changing ratio between orthoexcitons that make 1s-3p transitions and paraexcitons that make 1s-2p transitions. Because orthoexcitons have a shorter time of creation and a shorter lifetime, when time evolves the number of paraexcitons divided by the number of orthoexcitons will grow. This means that the position of the broad peak which consists of 1s-2p paraexciton absorption and 1s-3p orthoexciton absorption will shift to lower energies.

In figure 4.8 the intensities of the 1s-2p ortho, 1s-3p ortho and 1s-2p para transitions are shown as a function of time. These lie at energies of 116.7, 131, and



(a) Differential transmission spectra for different times.

(b) Shift of the peak position as a function of time.

Figure 4.7: Differential transmission spectra for sample K. Measurements were done in the visible pump - IR probe setup. Incident power: 10 mW (energy density 1 mJ/cm²), temperature 8 K, excitation wavelength 800 nm.

128.8 meV, respectively. We can see that paraexcitons are not present immediately. It takes about 300 ps for the paraexciton signal to reach its maximum value. Orthoexcitons on the other hand are created immediately. From this we can see that we create 1s orthoexcitons which are converted to paraexcitons. Since orthoexciton decay depends on the orthoexciton density, we cannot determine exactly when the paraexciton density is maximum. We can only say that it takes more than 300 ps.

In figure 4.9 the integrated intensity of the peak is plotted for three different pump powers. The higher the pump power, the higher is the intensity in the first 1.5 ns. But after 1.5 ns the intensity is the same for every pump power. Also the decrease in intensity in time is the same. This means that the amount of paraexcitons created is independent of pump power, although for higher pump power more orthoexcitons are created, because more photons are absorbed. Also, for higher pump powers more background energy has to be released.

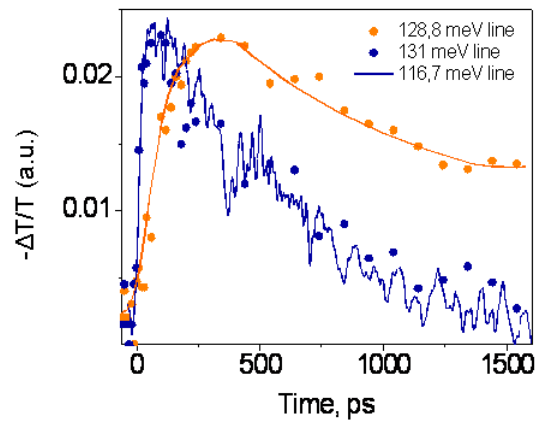


Figure 4.8: Kinetics of 1s-2p ortho transition (116.7 meV), 1s-2p para transition (128.8 meV) and 1s-3p ortho transition (131 meV). The excitation wavelength was 600 nm. The paraexciton signal needs some time to grow, while the orthoexciton signal is present immediately. This confirms that orthoexcitons and that paraexcitons are created through ortho-to-para conversion.

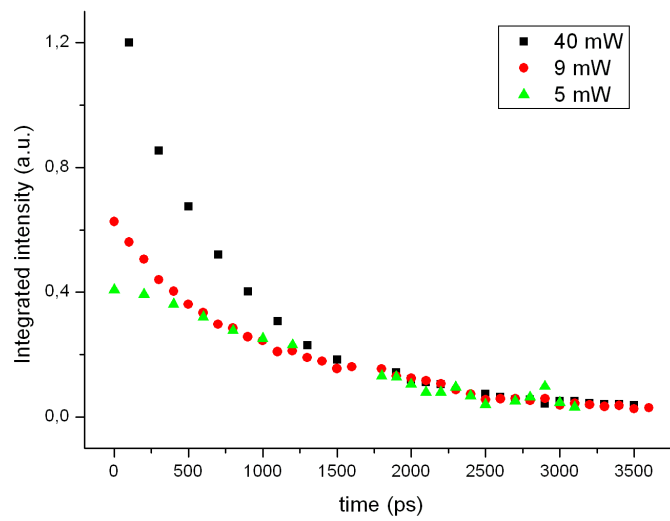


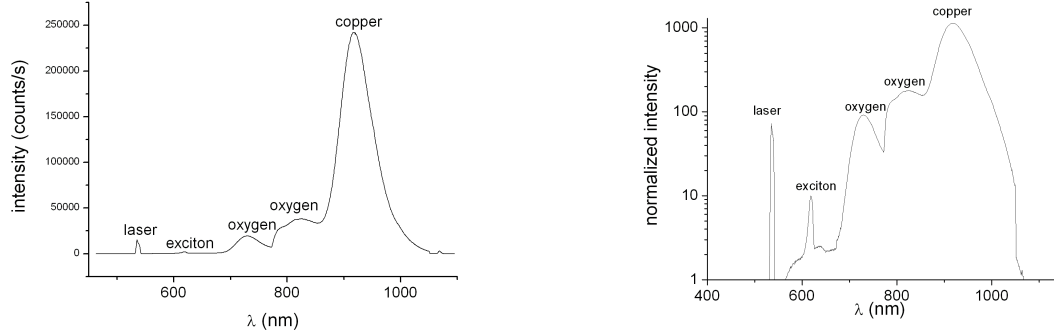
Figure 4.9: Integrated peak intensity for three different incident pump powers. The temperature is 6 K, the excitation wavelength 800 nm, and the sample thickness 500 μm . It can be seen that the amount of paraexcitons created does not depend on the initial incident power. The exciton density at later times is $10^{15}/\text{cm}^3$.

The penetration depth for 800 nm light is larger than for 605 nm light, which means that α is approximately constant through the sample for the small samples used. For 10 mW and 15 K we find an exciton density of about $5 \times 10^{16}/\text{cm}^3$ after 1.4 ps when most orthoexcitons have decayed. To reach Bose-Einstein condensation we need an exciton density which is two orders of magnitude higher at this temperature. For the conditions shown in figure 4.9 we calculated the density at later times to be in the order of $10^{15}/\text{cm}^3$ at this temperature. Again this is two orders of magnitude too small to reach BEC.

4.4 Vacancy measurements

Because of the high diffusion coefficient of excitons in Cu_2O (about $1000 \text{ cm}^2/\text{s}$ at 1.2 K) we expect a large influence of the vacancy concentration on the exciton lifetime. Therefore we decided to measure the vacancy concentration of the samples in the time-resolved luminescence setup to see if it can explain this difference. Figure 4.10 and 4.11 show the vacancy spectra of a sample with a short lifetime and a sample with a long lifetime. When we look at the intensity of the exciton peak we again see that it is much smaller, about an order of magnitude, for the sample with a short lifetime. If we assume that the intensity of the laser peak is linear with the laser power and is equal for different spectra when the incident power is equal, we can compare the ratio $I_{exciton}/I_{laser}$. For the short lifetime sample it is about 0.15 and for the long lifetime sample it is about 2.5.

A striking difference between the spectra is the intensity of the copper vacancy luminescence peak. For the short lifetime sample we see a large copper vacancy intensity. This means that possibly a lot of excitons are caught by a copper vacancy and decay from this vacancy to the ground state. This transition has a slightly lower energy than phonon-assisted decay, which explains why it can be seen at a slightly



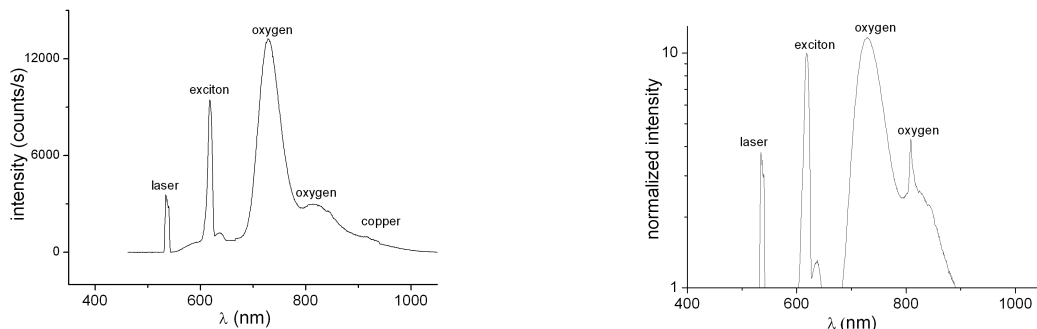
(a) Short lifetime vacancy spectrum. Incident power: 2 mW, sample thickness 360 μm .

(b) The same spectrum on a logarithmic scale. The spectrum is normalized such that $I_{exciton}$ is 10.

Figure 4.10: Vacancy spectra for sample C. Measurements were done in the time-resolved luminescence setup at 77 K. We used a grating with 150 grooves/mm. The excitation wavelength was 532 nm.

longer wavelength. For the long lifetime sample the copper vacancy intensity is almost zero. This observation can explain the lower exciton peak intensity of the short lifetime sample, since excitons that are trapped by a copper vacancy cannot contribute to the phonon-assisted exciton luminescence around 613 nm. For all the sample we measured we see that a large copper vacancy luminescence peak corresponds to a short lifetime and a small copper vacancy luminescence peak corresponds to a long lifetime.

Figure 4.12 shows that the ratio of the oxygen peak intensity divided by the exciton peak intensity for both oxygen peaks increases by about one order of magnitude when the lifetime decreases from the order of μs to ns. It is impossible to say from these measurements if the longer lifetime is partly due to a lower oxygen vacancy concentration, because the exciton luminescence peak decreases by about the same order of magnitude over this interval. The decrease in normalized inten-



(a) Long lifetime vacancy spectrum. Incident power: 2.5 mW, sample thickness 1 mm.

(b) The same spectrum on a logarithmic scale. The spectrum is normalized such that $I_{exciton}$ is 10.

Figure 4.11: Vacancy spectra for sample G. Measurements were done in the time-resolved luminescence setup at 77 K. We used a grating with 150 grooves/mm. The excitation wavelength was 532 nm.

sity for longer lifetimes is orders of magnitude lower than for the copper vacancy intensity, which suggests a weaker influence of oxygen vacancies on the exciton lifetime. More measurements need to be done to resolve this issue. Furthermore, we see that the oxygen peaks have approximately the same height relative to each other. It was calculated to be $I_{ox}^+/I_{ox}^{2+} = 2.5 \pm 2$. We conclude that the oxygen vacancy concentration does not seem to have a large influence on the exciton lifetime.

The reason for the correlation between copper vacancy luminescence intensity and exciton lifetime is not known yet. Also, it is unknown why oxygen vacancies do not seem to have a large influence on the exciton lifetime. It might be that the probability of an exciton being trapped by a copper vacancy is higher than being trapped by an oxygen vacancy. Another possibility is that the trapping to a copper vacancy is a faster process. Also, it might be valid to neglect the effect of oxygen vacancies because their concentration is lower. More experiments need to be done

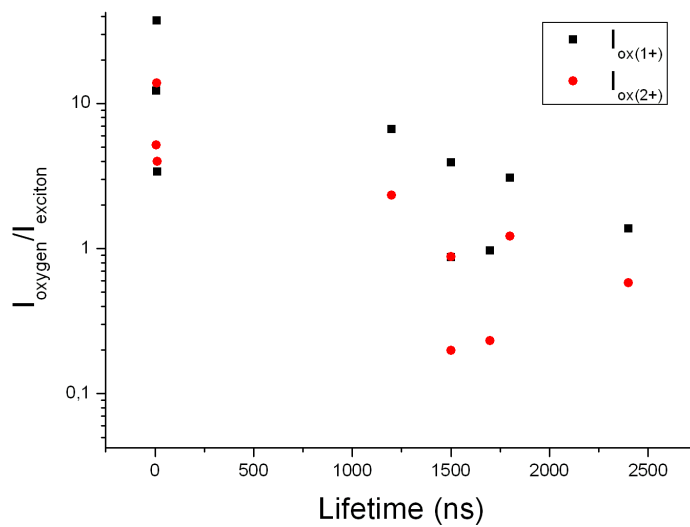


Figure 4.12: Oxygen vacancy luminescence intensity divided by exciton luminescence intensity as a function of lifetime. A decrease of about one order of magnitude in the ratio $I_{\text{ox}}/I_{\text{ex}}$ is seen when lifetimes increases from ns to μs . This is probably due to the increase of exciton peak intensity by about one order of magnitude over the same interval.

to reveal the mechanism by which vacancies influence the exciton lifetime.

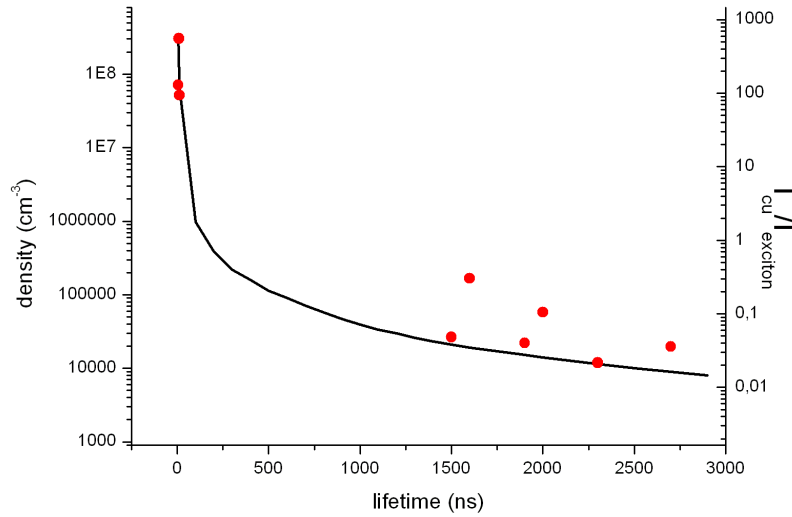


Figure 4.13: Copper vacancy concentration as a function of lifetime. The black line is calculated with equation 2.8. The red dots are taken from our measurements by calculating the ratio $I_{cu^-} / I_{exciton}$.

With equation 2.8 we estimate the vacancy concentration for different lifetimes. By looking at the ratio of $I_{cu^-} / I_{exciton}$ for every vacancy spectrum measured we can relate this ratio to a vacancy concentration. This is shown in figure 4.13. The simulation fits the measured ratio quite well. In conclusion, we have found that the copper vacancy concentration is directly related to the exciton lifetime. The higher the concentration, the shorter the lifetime will be.

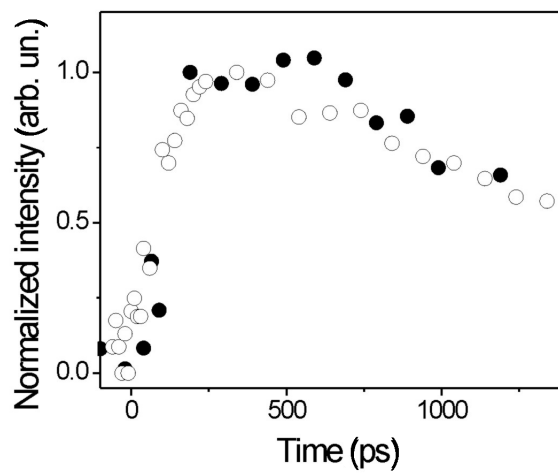


Figure 4.14: Early time dynamics of the 1s-2p paraexciton transition. Open circles: one-photon excitation with 2.07 eV, black circles: two-photon excitation with 1.55 eV. The curves have a similar shape, suggesting a similar paraexciton creation mechanism. The sample used was 200 μm thick and had (100) orientation. The temperature was 6 K. The energy density was 3 mJ/cm^2 .

4.5 Exciton density

Different methods of excitation may excite different excitonic states in Cu_2O with different efficiencies. For one-photon excitation first 1s orthoexcitons are created which can convert to paraexcitons. For two-photon absorption, excitons might be created by first exciting blue excitons, which decay via internal states to the 1s paraexciton level. Another difference between the excitation methods arises because of the difference in penetration depth. For 600 nm excitation, excitons are mainly created in the first 100 μm of the sample. For 800 nm excitation they are created in the whole sample and are distributed rather uniformly throughout the bulk.

In figure 4.14 the early time dynamics of the 1s-2p transition for both excitation methods is shown. For the two-photon excitation the broad background has been subtracted and kinetics have been normalized. We can see from the similarity of the curves that the formation kinetics for both cases are comparable. This suggests that both for one-photon and two-photon excitation the 1s paraexcitons are primarily created via down-conversion from the 1s orthoexciton level. The time constant of this process is at least 300 ps. Since a similar decay is observed for a penetration depth of 100 μm and excitation in the whole sample, the influence from the nearby surface in the one-photon excitation experiment seems to be negligible.

In figure 4.15 the 1s paraexciton density is plotted as a function of time for excitation with both 600 nm (black dots) and 800 nm light (orange dots). To calculate the paraexciton density (by using equation 2.28), the 1s orthoexciton contribution is deconvoluted from the total signal and subtracted. We can see that excitation with 600 nm leads to a higher exciton density. One reason for this is the difference in penetration depth for the two excitation wavelengths. For 800 nm excitation, excitons are created in the whole sample, which has a thickness of 200 μm . For 600 nm light the penetration depth is about 100 μm , so excitons are mainly created in

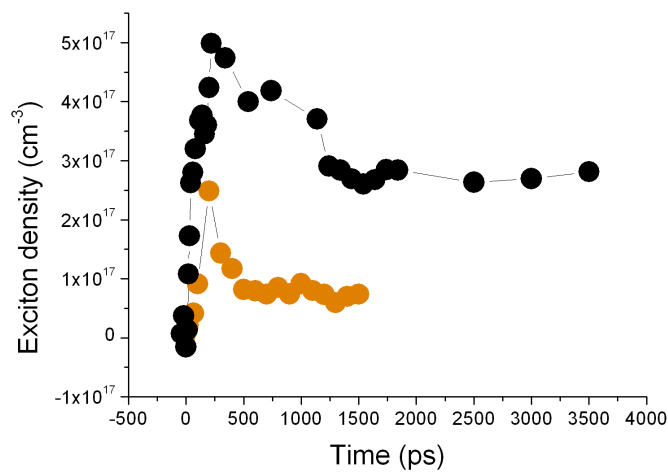


Figure 4.15: Exciton density as a function of time. The orange dots are for excitation with 800 nm light. The black dots are for excitation with 600 nm light. Because the penetration depth for 600 nm light is much smaller than for 800 nm light, the excitons are excited in a smaller part of the sample, which leads to a higher exciton density. The sample used was 200 μm thick and had (100) orientation. The temperature was 6 K. The energy density was 3 mJ/cm^2 .

the first half of the sample. This leads to an exciton density which is approximately twice as high in the first part of the sample. Another reason can be that the one-photon excitation process is more efficient. For exciton densities in the order of 10^{17} cm^{-3} , the temperature needed to reach Bose-Einstein condensation is about 2 K, which is experimentally feasible.

Chapter 5

Conclusion

In our experiments, we studied lifetime, luminescence and differential transmission of ortho and paraexcitons in different samples of Cu_2O . We also compared vacancy measurements for samples with short exciton lifetimes (in the order of ns) and long exciton lifetimes (in the order of μs). Below the conclusions for every kind of measurement will be summed.

Luminescence spectra analysis shows that the decay of orthoexcitons to the ground state is phonon-assisted mainly by the Γ_{12} phonon with a phonon energy of 13.6 meV. The temperature of the exciton gas is 80-85 K for all samples except one, which is considerably thicker than the others. Paraexcitons can be detected by their decay to the ground state via upconversion to orthoexcitons. No difference in lineshape is seen when the laser power is changed, which shows we are in the non-saturation excitation regime.

Lifetime measurements at 77 K reveal a set of samples with a lifetime in the order of 10 ns and a set of samples with a lifetime in the order of a few μs . Three different techniques are used for measuring lifetimes: time-resolved visible pump-infrared probe measurements, CW spectroscopy, and time-resolved luminescence

measurements. A reason for differences in lifetime is the difference in the amount of copper vacancies in the samples. Vacancy measurements show that the amount of vacancies in a sample is very important for the quality of the sample. The more vacancies are present, the shorter the lifetime will be. The reason why vacancies have such a huge influence is the large diffusion coefficient (about $1000 \text{ cm}^2/\text{s}$ at 1.2 K) of excitons in Cu_2O . When excitons come across a vacancy, they can get trapped. The mechanism for this process is not yet understood. We were able to fit our data with a diffusion model. For reasons that are still unknown, oxygen vacancies do not seem to have a large influence on the exciton lifetime.

Differential transmission for the 1s-2p para and 1s-3p orthoexciton peak was measured in two different setups. Both temperature and time dependence were measured. We see a peak shift to higher energy when temperature rises, which can be explained by a shifting of the excitonic levels that is different for different levels. We also see a peak shift, but to lower energy, when time evolves. This shift is caused by the decreasing ratio of ortho-to-para excitons, because orthoexcitons have a shorter lifetime and creation time than paraexcitons and the 1s-3p orthoexciton transition lies at slightly higher energy. Density calculations show that the paraexciton densities reached in the CW spectroscopy setup at initial times were about $5 \times 10^{16} \text{ cm}^{-3}$ at 15 K and 10^{15} cm^{-3} at 6 K for measurements with a short lifetime sample but a high incident power. These densities are more than 100 times too small to reach Bose-Einstein condensation at this temperature. The paraexciton density created does not depend on pump power.

As a recommendation, it might be interesting to measure the lifetime-temperature dependence of the paraexcitons. The upconversion process to orthoexcitons has a higher efficiency at higher temperatures, so paraexcitons can be detected easier. But we cannot be sure that the lifetime of the paraexcitons will be the same at different temperature. Also, it would be interesting to see if samples with even longer lifetime

can be produced, now we know which vacancies should be avoided.

To reach Bose-Einstein condensation, we need both high exciton density and low enough temperature. For this we need highly pure samples with a low copper vacancy concentration. Excitation should be done by intense laser pulses. We have reached an exciton density of about 10^{17} cm^{-3} in the time-resolved visible pump-infrared probe setup, which means that we need a temperature below 2.3 K. This is experimentally possible. Some of our samples have long enough lifetime to allow the paraexciton to cool down to the lattice temperature. So it might be possible to reach Bose-Einstein condensation in these samples.

Chapter 6

Acknowledgements

Doing research is a process in which many people are involved. Sharing thoughts and transferring knowledge are very important. During my master research a lot of help was available which I took advantage of gratefully. I would like to thank everybody who helped me in some way and the following people in particular.

In the first place Dmitry Fishman. He taught me a lot and was always willing to explain how things work. Although sometimes we did not understand each other perfectly because of cultural differences, I always felt that he wanted what was best for me. He has put a lot of effort and time in helping me becoming a good researcher, of which I can profit in my future work. He also taught me how to handle stress, by proposing a lot of changes for my Tokyo presentation just the evening before I had to give it.

Next I would like to thank my professor Paul van Loosdrecht. He helped me and Dmitry to stick to our planning. He helped us to analyze our data and improve our setup. And last but not least, he helped me to make the dream come true which I had had for a long time: visiting Japan to see how life is there and working in a well-equipped laboratory.

The people in Japan gave me a very warm welcome and helped me to start working on my own. I would like to thank professor Gonokami for giving me the opportunity to expand my knowledge and experience in his research group. Especially dr. Nobuko Naka was a big help for me. I am still amazed by the way she has organized her papers. She was able to give me a paper which contains the answer to my question in a few minutes, irrespective of which question I asked. Also, she made me feel comfortable and helped me with a lot of practical things I needed for living in a new city by myself. Mr. Yoshioka supervised me in doing the more complicated experiments and spent a lot of time completing my measurements when we could not finish in time. I also enjoyed the lunches with the members of the group and the nice conversations we had then. I had a wonderful time in Tokyo and I learned a lot about doing research and about myself.

I also would like to thank Pedro Rizo who helped me the first few months of my master research. He is a very good and patient teacher, and a very nice person to work with. Also thanks to Daniele Fausti for helping me with the Raman measurements.

Furthermore, the technical staff, especially Arjen Kamp, is very helpful in solving all kinds of problems. I am glad that we have people to do this for us, so we can focus on the physical part of experiments.

All the people of the optical condensed matter group were very nice to me. I am looking forward to becoming one of their colleagues next year. I am sure we will continue to have fun during coffee breaks, lunches and group outings.

My boyfriend Maarten Inklaar is always there to listen to my stories and frustrations. He helps me to see it all in perspective so I can find the courage to continue. He is one of the few persons who really understand me. Also, he understands the physics I am doing and is interested in my work. Since I have known him life is just much more fun.

Finally, I would like to thank my family and friends for the support and the nice times we spend together. These times give me a relaxed and happy feeling which has a positive influence on my work.

Bibliography

- [1] A. Mysyrowicz, D. Hulin, and A. Antonetti. Long Exciton Lifetime in Cu_2O . *Phys. Rev. Lett.*, 43(15):1123–1126, Oct 1979.
- [2] E.G. Gross and N.A. Karryev. *Doklady Akademii Nauk SSSR*, 84(261), 1952.
- [3] D. Snoke, JP Wolfe, and A. Mysyrowicz. Quantum saturation of a Bose gas: Excitons in Cu_2O . *Physical Review Letters*, 59(7):827–830, 1987.
- [4] KE OHara, L. Ó Súilleabháin, and JP Wolfe. Strong nonradiative recombination of excitons in Cu_2O and its impact on Bose-Einstein statistics. *Physical Review B*, 60(15):10565–10568, 1999.
- [5] GM Kavoulakis. Bose-Einstein condensation of excitons in Cu_2O . *Physical Review B*, 65(3):35204, 2001.
- [6] D. W. Snoke and J. P. Wolfe. Picosecond dynamics of degenerate orthoexcitons in Cu_2O . *Phys. Rev. B*, 42(13):7876–7884, Nov 1990.
- [7] A. Jolk, M. Jörger, and C. Klingshirn. Exciton lifetime, Auger recombination, and exciton transport by calibrated differential absorption spectroscopy in Cu_2O . *Phys. Rev. B*, 65(24):245209, Jun 2002.

- [8] K. Karpinska, M. Mostovoy, MA van der Vegte, A. Revcolevschi, and PHM van Loosdrecht. Decay and coherence of two-photon excited yellow orthoexcitons in Cu_2O . *Physical Review B*, 72(15):155201, 2005.
- [9] K. Reimann and K. Syassen. Raman scattering and photoluminescence in Cu_2O under hydrostatic pressure. *Phys. Rev. B*, 39(15):11113–11119, May 1989.
- [10] KE OHara and JP Wolfe. Relaxation kinetics of excitons in cuprous oxide. *Physical Review B*, 62(19):12909–12922, 2000.
- [11] T. Fleck, M. Jrger, and C. Klingshirn. Exciton transport and intersubband transitions in Cu_2O . *Physica status solidi (C)*, 3(7):2473–2476, 2006.
- [12] T. Fleck. Laserinduzierte Absorptionsänderungen in Cu_2O . *Dissertation*, 2005.
- [13] C. Uihlein, D. Fröhlich, and R. Kenklies. Investigation of exciton fine structure in Cu_2O . *Physical Review B*, 23(6):2731–2740, 1981.
- [14] M. Kuwata-Gonokami, M. Kubouchi, R. Shimano, and A. Mysyrowicz. Time-resolved Excitonic Lyman Spectroscopy of Cu_2O . *Journal of the Physical Society of Japan*, 73(4):1065–1069, 2004.
- [15] K. Karpinska, PHM van Loosdrecht, IP Handayani, and A. Revcolevschi. Paraexcitons in Cu_2O a new approach. *Journal of Luminescence*, 112(1-4):17–20, 2005.
- [16] M. Jörger, T. Fleck, C. Klingshirn, and R. von Baltz. Midinfrared properties of cuprous oxide: High-order lattice vibrations and intraexcitonic transitions of the 1s paraexciton. *Physical Review B*, 71(23):235210, 2005.
- [17] R.L. Liboff. Introductory quantum mechanics. *Addison Wesley*, 2003.

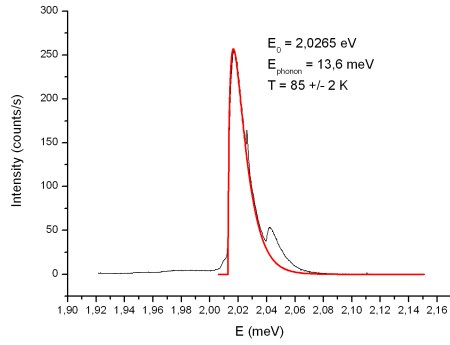
- [18] Y. Liu and D. Snoke. Resonant two-photon excitation of 1s paraexcitons in cuprous oxide. *Solid State Communications*, 134(1-2):159–164, 2005.
- [19] T. Ito, H. Yamaguchi, K. Okabe, and T. Masumi. Single-crystal growth and characterization of Cu_2O and CuO . *Journal of Materials Science*, 33(14):3555–3566, 1998.
- [20] DP Trauernicht and JP Wolfe. Drift and diffusion of paraexcitons in Cu_2O : Deformation-potential scattering in the low-temperature regime. *Physical Review B*, 33(12):8506–8521, 1986.
- [21] J Bloem. Discussion of some optical and electrical properties of Cu_2O . *Philips Res. Repts*, 13:167–193, 1958.
- [22] N.A. Tolstoi and V.A. Bonch-Bruевич. Luminescence of oxygen vacancies in cuprous oxide. *Soviet Physics - Solid state*, 13(5):1135–1137, 1971.
- [23] M. Yan, L. J. Rothberg, F. Papadimitrakopoulos, M. E. Galvin, and T. M. Miller. Defect Quenching of Conjugated Polymer Luminescence. *Phys. Rev. Lett.*, 73(5):744–747, Aug 1994.
- [24] B. Ya. Balagurov and V. G. Vaks. Random walks of a particle on lattices with traps. *Sov. Phys. JETP*, 38(5), 1974.
- [25] YP Varshni. Temperature dependence of the energy gap in semiconductors. *PHYSICA*, 34(1):149–154, 1967.
- [26] S. Logothetidis, M. Cardona, P. Lautenschlager, and M. Garriga. Temperature dependence of the dielectric function and the interband critical points of CdSe . *Phys. Rev. B*, 34(4):2458–2469, Aug 1986.

- [27] D. W. Snoke, A. J. Shields, and M. Cardona. Phonon-absorption recombination luminescence of room-temperature excitons in Cu_2O . *Phys. Rev. B*, 45(20):11693–11697, May 1992.
- [28] A Griffin, D.W. Snoke, and S. Stringari. Bose-Einstein condensation. *Cambridge University Press*, 1995.
- [29] T Ideguchi. Master Thesis. *The university of Tokyo*, 2006.
- [30] K. Yoshioka, T. Ideguchi, and M. Kuwata-Gonokami. Laser-based continuous-wave excitonic Lyman spectroscopy in Cu_2O . *To be published*, 2007.

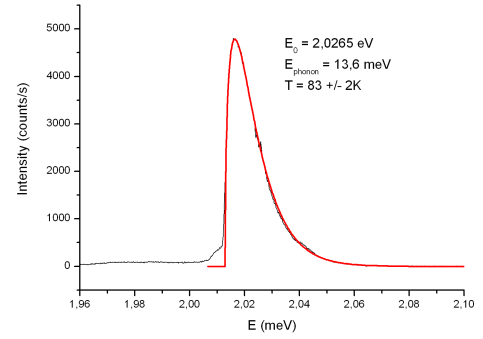
Appendix A

Luminescence

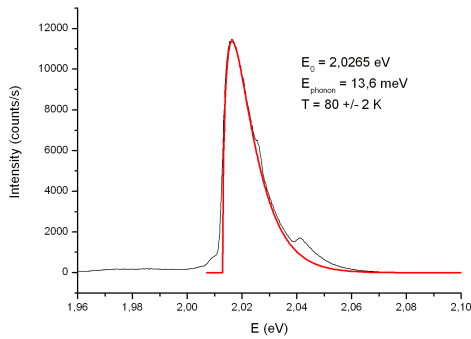
Below luminescence spectra of all the samples, which are not shown in the results, are depicted. These are measured at a lattice temperature of 77 K in transmission mode. We used a grating with 1200 grooves/mm. The excitation wavelength was 800 nm, which means that excitons are excited by a two photon absorption process. The black curve is the signal and the red curve is the fit.



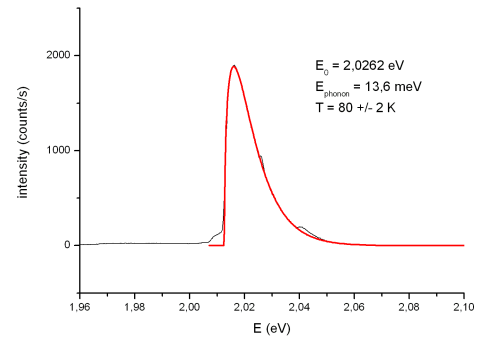
(a) Sample A. Incident power: 18.5 mW (energy density 15 mJ/cm²), sample thickness 140 μm .



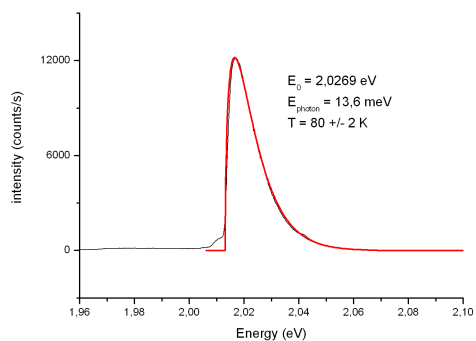
(b) Sample B. Incident power: 8.3 mW (energy density 6.8 mJ/cm²), sample thickness 765 μm .



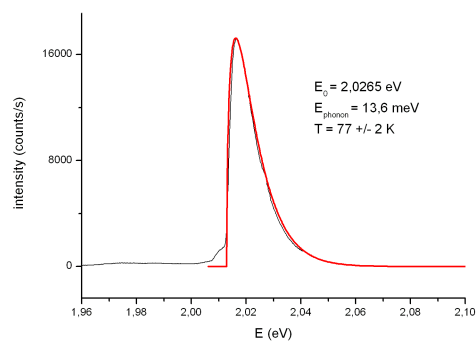
(c) Sample C. Incident power: 75 mW (energy density 61 mJ/cm²), sample thickness 360 μm .



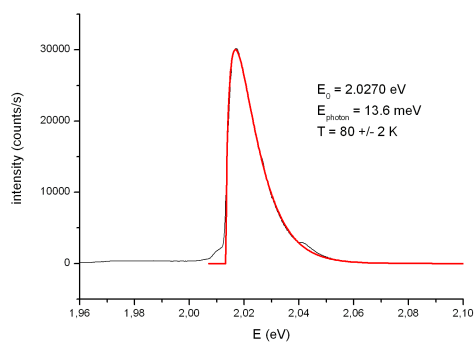
(d) Sample F. Incident power: 7 mW (energy density 5.7 mJ/cm²), sample thickness 220 μm .



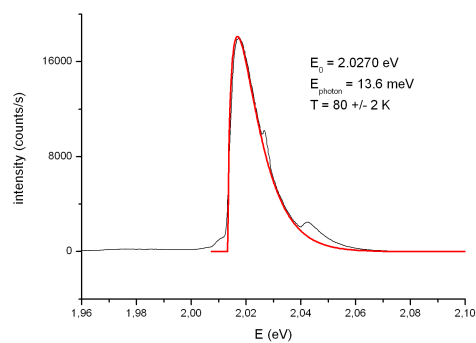
(e) Sample G. Incident power: 2 mW (energy density 1.6 mJ/cm²), sample thickness 1 mm.



(f) Sample H. Incident power: 2.5 mW (energy density 2.0 mJ/cm²), sample thickness 2.5 mm.



(g) Sample I. Incident power: 2 mW (energy density 1.6 mJ/cm²), sample thickness 960 μ m.

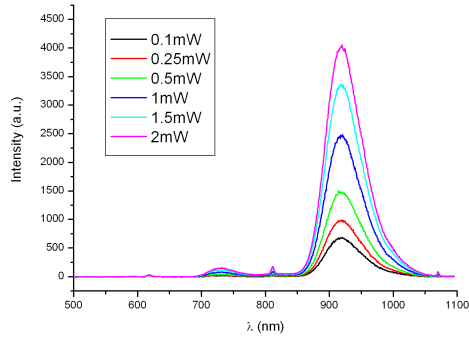


(h) Sample J. Incident power: 0.9 mW (energy density 0.8 mJ/cm²), sample thickness 400 μ m.

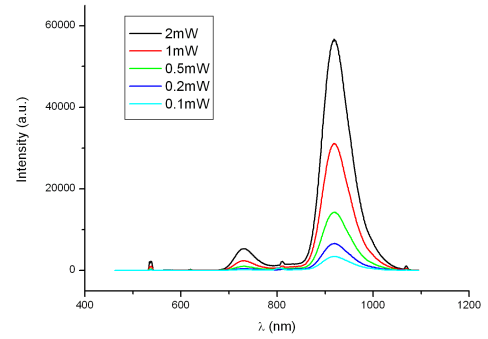
Appendix B

Vacancies

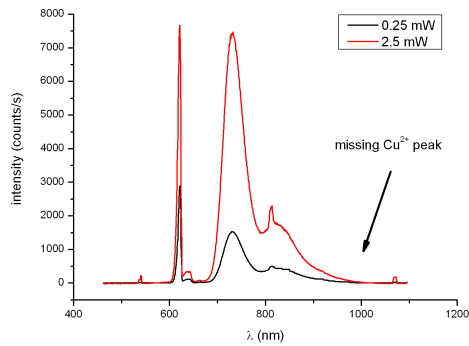
Below vacancy spectra of all the samples, which are not shown in the results, are depicted. These are measured at a lattice temperature of 77 K in reflection mode. We used a grating with 150 grooves/mm. The excitation wavelength was 532 nm, which means that excitons are excited by a one photon absorption process.



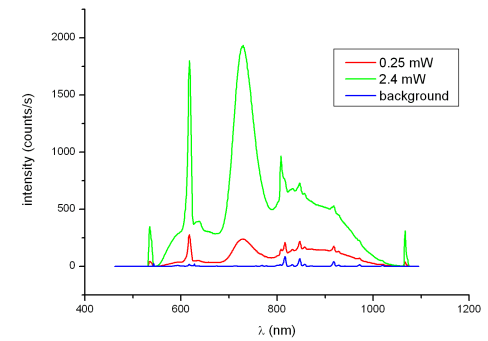
(a) Vacancy spectrum for different laser powers for sample B. Sample thickness $765 \mu\text{m}$.



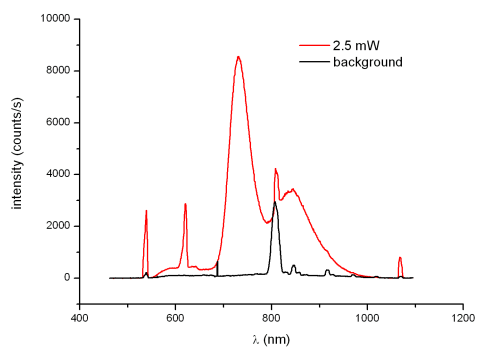
(b) Vacancy spectrum for different laser powers for sample D. Sample thickness $375 \mu\text{m}$.



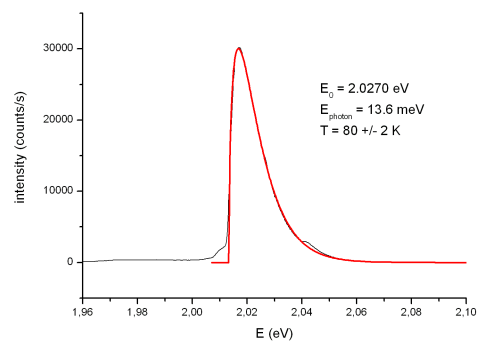
(c) Vacancy spectrum for different laser powers for sample E. Sample thickness $220 \mu\text{m}$. The peak around 820 nm is caused by background radiation.



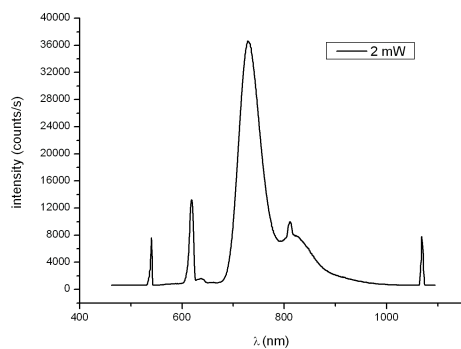
(d) Vacancy spectrum for different laser powers for sample F. Sample thickness $220 \mu\text{m}$.



(e) Vacancy spectrum for a laser power of 2.5 mW for sample H. Sample thickness 2.5 mm.



(f) Vacancy spectrum for a laser power of 2 mW for sample I. Sample thickness 960 μm .

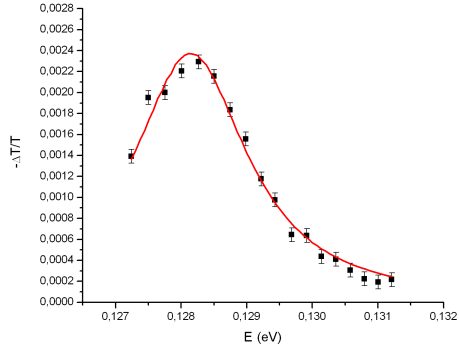


(g) Vacancy spectrum for a laser power of 2 mW for sample J. Sample thickness 400 μm .

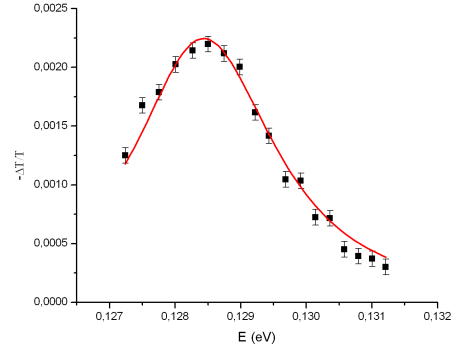
Appendix C

Differential transmission

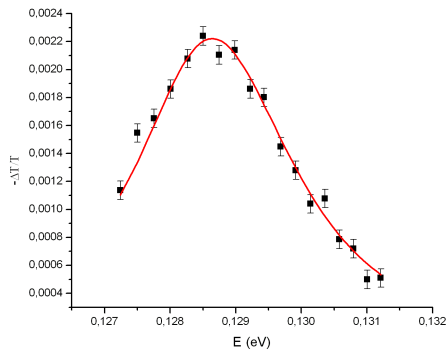
Below differential transmission spectra for sample H for different temperatures are shown. The excitation wavelength was 605 nm, which means that excitons are excited by a one photon absorption process. The thickness of the sample was $\approx 2500 \mu\text{m}$. The energy density was $2.5 \mu\text{J}/\text{cm}^2$. The black dots are the experimental values and the red curve is the fit. The formulas fitting are described in section 4.3. In the table the important fitting parameters for different temperatures are indicated.



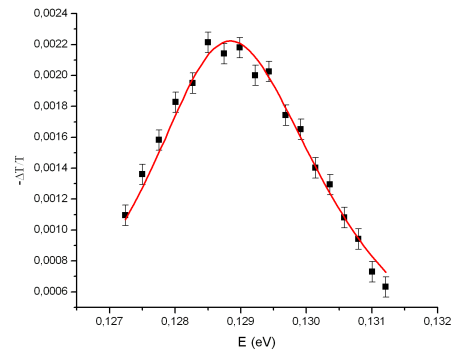
(a) Differential transmission spectrum for $T = 5$ K.



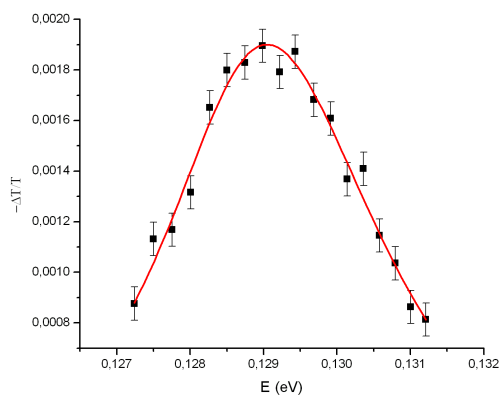
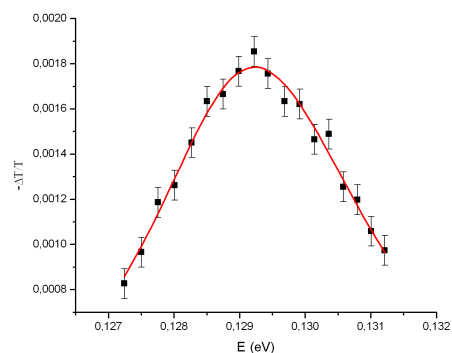
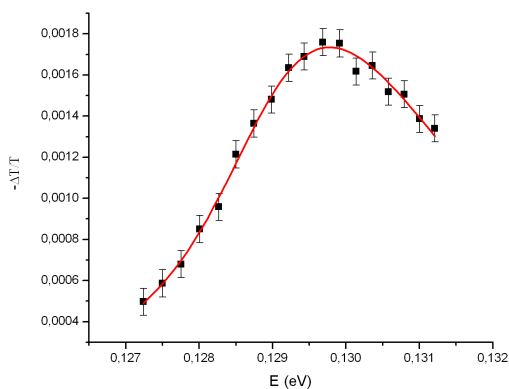
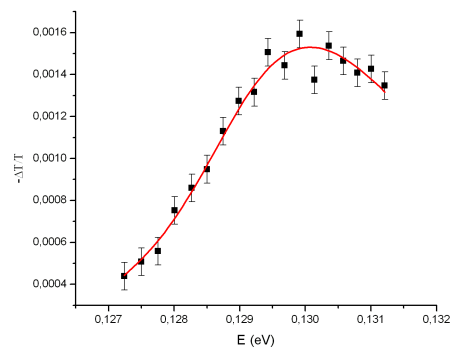
(b) Differential transmission spectrum for $T = 10$ K.

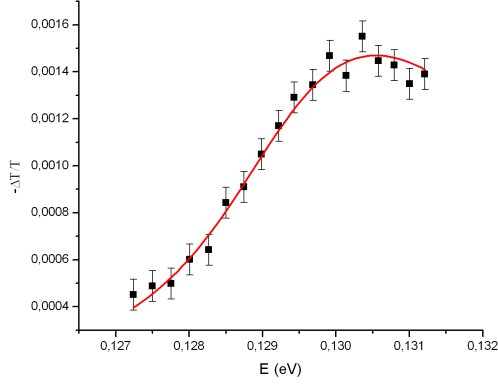
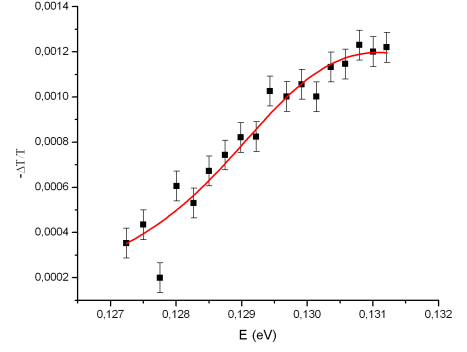


(c) Differential transmission spectrum for $T = 15$ K.



(d) Differential transmission spectrum for $T = 20$ K.

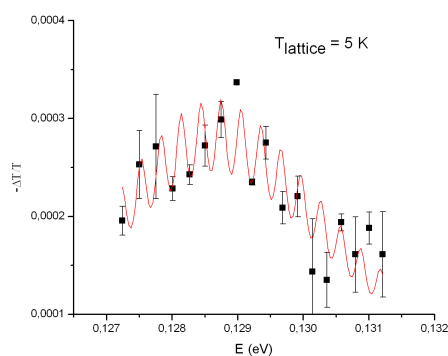
(e) Differential transmission spectrum for $T = 25$ K.(f) Differential transmission spectrum for $T = 30$ K.(g) Differential transmission spectrum for $T = 35$ K.(h) Differential transmission spectrum for $T = 40$ K.

(i) Differential transmission spectrum for $T = 50$ K.(j) Differential transmission spectrum for $T = 60$ K.

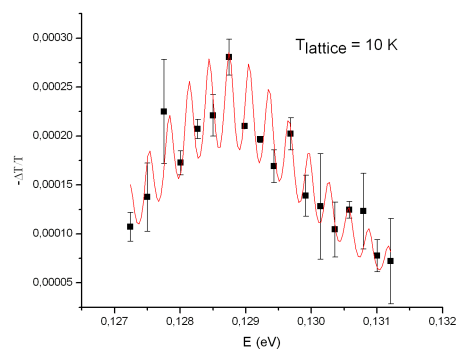
Temperature (K)	$\Gamma/2$ (eV)	m_s/m_p
5	0.00103	1.23
10	0.00119	1.28
15	0.00130	1.26
20	0.00142	1.24
25	0.00153	1.24
30	0.00175	1.22
35	0.00127	1.39
40	0.00142	1.41
50	0.00153	1.41
60	0.00189	1.41

Table C.1: Fitting parameters for sample H.

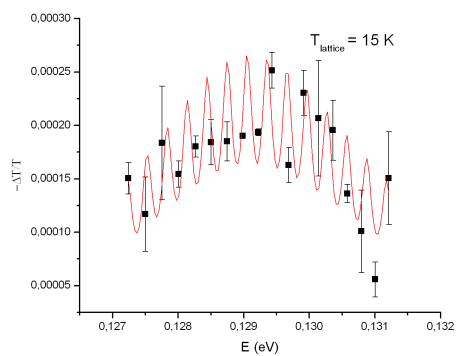
Below differential transmission spectra for sample B for different temperatures are shown. The excitation wavelength was 605 nm, which means that excitons are excited by a one photon absorption process. The thickness of the sample was 765 μm . The energy density was 6.3 mJ/cm². The black dots are the experimental values and the red curve is a simulated curve that roughly fits the data. The formulas for the simulation are described in section 4.3. In the table the important simulation parameters for different temperatures are indicated.



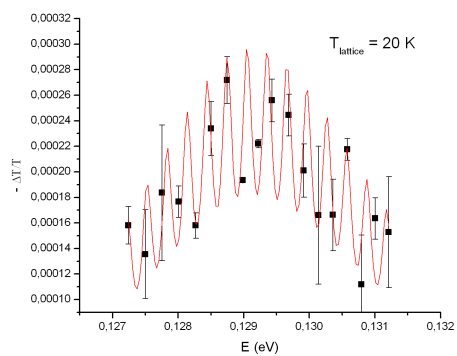
(a) Differential transmission spectrum for $T = 5$ K.



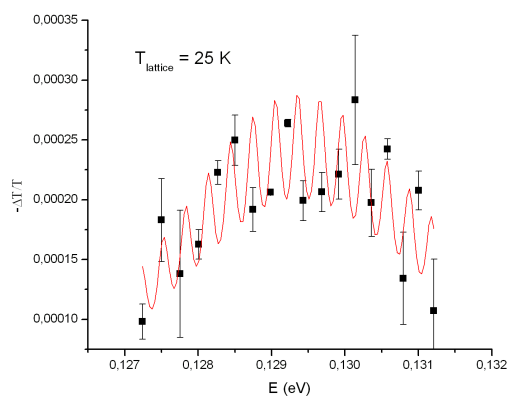
(b) Differential transmission spectrum for $T = 10$ K.



(c) Differential transmission spectrum for $T = 15$ K.



(d) Differential transmission spectrum for $T = 20$ K.



(e) Differential transmission spectrum for $T = 25$ K.

Temperature (K)	$T_{exciton}$ (K)	ΔE (eV)	$\Gamma/2$ (eV)	m_s/m_p	κ
5	15.5	0.12822	0.00223	1.22717	0.00095
10	15.3	0.12821	0.00147	1.28321	0.00048
15	25.6	0.12841	0.00197	1.24426	0.00034
20	26.5	0.12843	0.00198	1.24426	0.00032
25	31.9	0.12855	0.00196	1.2359	0.00062

Table C.2: Simulation parameters for sample B.